

CHESTER F. CARLSON
CENTER FOR IMAGING SCIENCE
COLLEGE OF SCIENCE
ROCHESTER INSTITUTE OF TECHNOLOGY
ROCHESTER, NEW YORK

CERTIFICATE OF APPROVAL

M.S. DEGREE THESIS

The M.S. Degree Thesis of Nancy L. Baccheschi
has been examined and approved by the
thesis committee as satisfactory for the
thesis requirement for the
Master of Science degree

Dr. John Schott

Dr. John Kerekes

Mr. Scott Brown

Date

Report Documentation Page

Form Approved
OMB No. 0704-0188

Public reporting burden for the collection of information is estimated to average 1 hour per response, including the time for reviewing instructions, searching existing data sources, gathering and maintaining the data needed, and completing and reviewing the collection of information. Send comments regarding this burden estimate or any other aspect of this collection of information, including suggestions for reducing this burden, to Washington Headquarters Services, Directorate for Information Operations and Reports, 1215 Jefferson Davis Highway, Suite 1204, Arlington VA 22202-4302. Respondents should be aware that notwithstanding any other provision of law, no person shall be subject to a penalty for failing to comply with a collection of information if it does not display a currently valid OMB control number.

1. REPORT DATE 05 OCT 2005	2. REPORT TYPE N/A	3. DATES COVERED -						
4. TITLE AND SUBTITLE Generation of a Combined Dataset of Simulated Radar and Electro-Optical Imagery								
5a. CONTRACT NUMBER 								
5b. GRANT NUMBER 								
5c. PROGRAM ELEMENT NUMBER 								
6. AUTHOR(S) 								
5d. PROJECT NUMBER 								
5e. TASK NUMBER 								
5f. WORK UNIT NUMBER 								
7. PERFORMING ORGANIZATION NAME(S) AND ADDRESS(ES) Rochester Institute Of Technology Rochester, New York								
8. PERFORMING ORGANIZATION REPORT NUMBER 								
9. SPONSORING/MONITORING AGENCY NAME(S) AND ADDRESS(ES) The Department of the Air force AFIT/CIA, Bldg 125 WPAFB, OH 45433								
10. SPONSOR/MONITOR'S ACRONYM(S) 								
11. SPONSOR/MONITOR'S REPORT NUMBER(S) 								
12. DISTRIBUTION/AVAILABILITY STATEMENT Approved for public release, distribution unlimited								
13. SUPPLEMENTARY NOTES The original document contains color images.								
14. ABSTRACT 								
15. SUBJECT TERMS 								
16. SECURITY CLASSIFICATION OF: <table style="width: 100%; border-collapse: collapse;"> <tr> <td style="width: 33%; text-align: center;">a. REPORT unclassified</td> <td style="width: 33%; text-align: center;">b. ABSTRACT unclassified</td> <td style="width: 34%; text-align: center;">c. THIS PAGE unclassified</td> </tr> </table>			a. REPORT unclassified	b. ABSTRACT unclassified	c. THIS PAGE unclassified	17. LIMITATION OF ABSTRACT UU	18. NUMBER OF PAGES 89	19a. NAME OF RESPONSIBLE PERSON
a. REPORT unclassified	b. ABSTRACT unclassified	c. THIS PAGE unclassified						

THESIS RELEASE PERMISSION
ROCHESTER INSTITUTE OF TECHNOLOGY
COLLEGE OF SCIENCE
CHESTER F. CARLSON
CENTER FOR IMAGING SCIENCE

Generation of a Combined Dataset of Simulated Radar and Electro-Optical Imagery

I, Nancy L. Baccheschi, do hereby grant permission to the Wallace Memorial Library of RIT to reproduce my thesis in whole or in part. Any reproduction will not be for commercial use or profit.

Signature: _____

Date: _____

Generation of a Combined Dataset of Simulated Radar and Electro-Optical Imagery

by
Nancy L. Baccheschi

Submitted to the
Chester F. Carlson Center for Imaging Science
in partial fulfillment of the requirements
for the Master of Science Degree
at the Rochester Institute of Technology

ABSTRACT

In the world of remote sensing there exist radar sensors and EO/IR sensors, both of which carry with them unique information useful to the imaging community. Radar has the capability of imaging through all types of weather, day or night. EO/IR produces radiance maps and frequently images at much finer resolution than radar. While each of these systems is valuable to imaging, there exists unknown territory in the imaging community as to the value added in combining the best of both these worlds. This work will begin to explore the challenges in simulating a scene in both a radar tool called Xpatch and an EO/IR tool called DIRSIG. The capabilities and limitations inherent to both radar and EO/IR are similar in the image simulation tools, so the work done in a simulated environment will carry over to the real-world environment as well. The synthetic data generated will be compared to existing measured data to demonstrate the validity of the experiment. Future work should explore registration and various types of fusion of the resulting images to demonstrate the synergistic value of the combined images.

Disclaimer

The views expressed in this thesis are those of the author and do not reflect the official policy or position of the United States Air Force, Department of Defense, or the U.S. Government.

Acknowledgements

I would like to take this opportunity to thank my thesis committee, Dr. John Schott, Dr. John Kerekes and Mr. Scott Brown, for their support and guidance in my graduate studies over the past year. I would also like to thank all the other students, faculty and staff in the DIRS department for your continued assistance. I would still be trying to pass Roger's class and get my first DIRSIG run going if it weren't for the help you all gave me. Thanks to all the other Air Force students and their families for not only helping me in my efforts at RIT, but for making non work-related activities enjoyable as well, including the infamous (and sometimes logistically insufferable) "Lunch Day". Specifically, I'd like to thank Dan Blevins, who patiently taught me more stuff than I'll ever need to know about SAR. I would like to extend a special thanks to Cindy Schultz, without whom I would have never been able to track down my thesis advisor, and who continually helped me with things not even closely related to her job description. Also, thanks to Cindy for making me laugh when I was stressed out and convinced that I would be the first Air Force student to leave here without a degree.

Dedication

This work is dedicated to my family, specifically my mom and Earl, for supporting me in everything I've done with my life so far. Thank you to Mike as well for helping me to "build character" all these years and making sure I had a well-balanced diet...fuzzy dandelions really are healthy.

Table of Contents

1	<i>Introduction</i>	1
2	<i>Background and Theory</i>	3
2.1	Optical Radiation Propagation	3
2.1.1	Propagation of Energy	3
2.1.2	Radiometric Terms	6
2.1.3	Electro-Optical Imaging	7
2.2	Radar Fundamentals	10
2.2.1	Basic Radar Concept	10
2.2.2	Real Aperture Radar Imaging	12
2.3	SAR Fundamentals	17
2.3.1	Basic SAR Concept	17
2.3.2	Sidelobes	19
2.3.3	Resolution	19
2.3.4	Phase Correction	20
2.3.5	Motion Compensation	22
2.3.6	Signal Phase Equation	22
2.4	DIRSIG	25
2.5	Xpatch	29
2.5.1	Xpatch Overview	29
2.5.2	Pre- and Post-Processing Tools	34
2.5.3	ModelMan	36
2.5.4	Pioneer	37
3	<i>Experimental Design</i>	40
3.1	YOGI Experiment	40
3.1.1	Sensors	42
3.2	Common Scene Development	44
3.3	Basic Scene Development for DIRSIG	45
3.4	Basic Scene Development for Xpatch	48

4	<i>Results</i>	51
4.1	Electro-Optical Scene Comparisons	51
4.1.1	DIRSIG Response Files	51
4.1.2	Texturization	52
4.1.3	Transmissive Materials	55
4.1.4	Aircraft Motion Smear.....	56
4.1.5	Point Spread Functions	57
4.1.6	Spectral Comparisons	58
4.2	Synthetic Aperture Radar Scene Comparisons	62
4.2.1	CAD Conversion.....	63
4.2.2	Material Attribution	63
4.2.3	Platform Configuration	64
4.2.4	IFSAR Calibration	64
4.2.5	SAR Profile Comparisons.....	64
5	<i>Conclusions</i>	72
5.1	Electro-Optical Simulations	72
5.2	Synthetic Aperture Radar Simulations	73
5.3	Data Fusion	75
5.4	Recommendations for Future Work	75
6	<i>References</i>	77

List of Figures

Figure 2.1-1 – Solar Energy Paths (Schott, 1997)	3
Figure 2.1-2 – Self-emitted thermal energy paths (Schott, 1997)	4
Figure 2.1-3 – Line Scanner design, with liquid nitrogen cooling for thermal bands (Schott, 1997)	9
Figure 2.1-4 – Push-broom design (Schott, 1997)	10
Figure 2.2-1 – Illustration of backscatter (NASA JPL, 1996).....	11
Figure 2.2-2 - Backscatter return for surfaces of different texture (NASA JPL, 1996).....	14
Figure 2.2-3 - Illustration of a corner reflector, such as a building intersecting a street.....	15
Figure 2.3-1 – Block diagram of a SAR system (Richards, 2003).....	17
Figure 2.3-2 – Stripmap-mode SAR imaging (Richards, 2003).....	18
Figure 2.3-3 – Spotlight-mode SAR imaging (Richards, 2003).....	18
Figure 2.3-4 – Radar beam sidelobes (Integrated Publishing, 2004).....	19
Figure 2.3-5 – SAR image formation block diagram (Blevins, 2004).....	24
Figure 2.4-1 – DIRSIG ray tracing (Peterson, 2004).....	27
Figure 2.4-2 – DIRSIG submodel interactions (Peterson, 2004)	28
Figure 2.5-1 – Illustration of facet requirement for curved surfaces.....	31
Figure 2.5-2 – Xpatch outputs (SAIC, 2004).....	32
Figure 2.5-3 – XEdge GUI (SAIC, 2004)	34
Figure 2.5-4 – Xyplot display window (SAIC, 2004)	35
Figure 2.5-5 – McImage display window (SAIC, 2004)	35
Figure 2.5-6 – XSignal display window (SAIC, 2004)	36
Figure 2.5-7 – ModelMan display window (SAIC, 2004).....	36
Figure 2.5-8 – Pioneer display window (SAIC, 2004)	38
Figure 3.1-1 – NRL WAR HORSE (Courtesy of Space Computer, 2004)	43
Figure 3.2-1 – Model of corner reflector.....	45
Figure 3.2-2 – Scene used for simulations.	45
Figure 3.3-1 – Model of 16-foot corner	46
Figure 3.3-2 – Actual 16-foot corner reflector.....	46
Figure 3.3-4 – Model of 15" corner reflector.....	46
Figure 3.3-4 – Actual 15" corner reflector.....	46
Figure 3.3-5 – Flow chart of DIRSIG configuration file.....	48
Figure 3.4-1 – Flow chart of Xpatch input file	50
Figure 4.1-1 – Flow diagram of texture application in DIRSIG (DIRSIG User's Manual, 2004)	53
Figure 4.1-2 – Vegetation reflectance curves used for DIRSIG texture map	54
Figure 4.1-3 - Rendered electro-optical scene from DIRSIG with ideal aircraft velocity	59
Figure 4.1-4 – DIRSIG corner reflector with smear due to aircraft motion	59
Figure 4.1-5 – WARHORSE corner reflector	59
Figure 4.1-6 – Corner Reflector Spectral Comparison (RMSE = 3.01%)	60
Figure 4.1-7 – Grass Spectral Comparison (RMSE = 2.85%)	60
Figure 4.1-8 – Tree Spectral Comparison (RMSE = 3.41%)	60
Figure 4.1-9 – CR spectral comparison for shifted data (RMSE = 2.19%)	61
Figure 4.1-10 – Grass spectral comparison for shifted data (RMSE = 2.21%)	61
Figure 4.1-11 – Tree spectral comparison for shifted data (RMSE = 3.24%)	62
Figure 4.2-1 – WARHORSE (left) and IFSAR (right) images of Fisher Creek.....	66
Figure 4.2-2 - IFSAR with corner reflector in zoomed box (left and middle) and Xpatch SAR for 16° corner reflector in free space	66
Figure 4.2-3 – Xpatch and IFSAR data comparisons	67
Figure 4.2-4 – Single slice Xpatch and IFSAR comparison (RMSE = 2.28%)	67
Figure 4.2-5 – Effects of different windowing techniques	69
Figure 4.2-7 – Xpatch SAR image for radar pointed at side panel	70
Figure 4.2-8 – Example of bright returns from corner reflectors (NPA Satellite Mapping, 2005)	71

List of Tables

Table 2.5-1 - Example Radar Frequencies with Object Sizes	33
Table 3.1-1 – WAR HORSE specifications (Space Computer, 2004 and Orloff et al, March 2004).....	43
Table 3.1-2 – NRL IFSAR specifications (Orloff et al, March 2004)	44

1 Introduction

Remote sensing has been an ongoing effort for decades, both in electro-optical/infrared (EO/IR) imaging and radar imaging. Many advances in technology have led to better resolution, increased spatial and spectral coverage, faster analysis of the collected images, and automated means by which to perform certain types of analysis on the data. While there has been an extensive amount of work done in radar and EO/IR imaging separately, there has been less work done in combining the technologies.

Radar offers information, such as ranging and dielectric properties, that EO/IR imaging does not. Furthermore, it can penetrate many types of weather, including rain, clouds and fog and it can be used to image day or night. Radar can also penetrate foliage to detect targets that may be obscured from overhead. On the other hand, EO/IR imaging affords the user information about inherent optical properties, such as reflectivity, emissivity or radiance values. It tends to have much finer spatial resolution than radar and is capable of small object target detection, but is limited by weather, daytime imaging conditions (except in the case of thermal infrared, which can image at night), and often can only image at or near nadir viewing geometry. With these advantages and disadvantages of both types of imaging systems, it is reasonable to expect that combining the two systems in some way, whether as one sensor or by fusing resulting images, might yield more information than either one alone (Hsu et al, 1999).

Obtaining actual radar or EO/IR data can be costly and time-consuming for such purposes as exploring fusion techniques. Therefore, it makes sense to take advantage of image simulation tools, such as Xpatch for radar and DIRSIG (Digital Imaging and Remote Sensing Image Generation) for EO/IR (DIRSIG Manual, 2004). DIRSIG is an image generation model developed by the Digital imaging and Remote Sensing (DIRS) Laboratory at the Rochester Institute of Technology. It is capable of producing simulated imagery in the regions spanning visible to infrared (DIRSIG Manual, 2004). Xpatch is a similar image generation tool except that it simulates imagery in the radar region. It was developed by DEMACO, Inc, which is now part of SAIC (SAIC website, 2001). Much work can be done using simulated data to test algorithms or theories before spending the resources on the real data only to determine that the algorithm or theory was invalid (DIRSIG Manual, 2004).

The purposes of this project are to produce valid computer-aided design (CAD) geometries for a scene, correctly render that scene in both Xpatch and DIRSIG from a common geometry, and compare the synthetic data to measured data. The next step would be to fuse or register the images and determine the synergistic value of the combined images versus the

individual ones. It is of critical importance to correctly model the geometry in both tools so that the resulting scenes are accurate.

The challenges encountered and documented in building the CAD models and obtaining accurate synthetic data in both tools should help further the research in the area of combining EO/IR and radar data. When many of those challenges are worked through and it is possible to fuse the images, the hope is that the end result of the combined images will be more valuable than each of the separate images. The distinct differences in results that each of the systems produces should generate a product that contains more information than could be had out of either of the separate images. Modeling tools can afford users the capability to explore sensor design trades, tasking trades, algorithm performance, algorithm testing, and other related tasks.

2 Background and Theory

This section affords the reader a background on the theory and fundamentals of the work to be performed. The section begins with a brief description of optical radiation propagation so that the reader has a basic understanding of various terms regarding the concepts that will be used throughout the rest of the document. A general overview of radar fundamentals, including synthetic aperture radar (SAR), will be incorporated in this section as well. Also, the image simulation tools for both radar and electro-optical imaging, Xpatch and DIRSIG, respectively, will be discussed.

2.1 Optical Radiation Propagation

In this section, the fundamental concepts of the energy paths of light will be discussed as well as the related radiometric terms. There will also be a discussion of electro-optical imaging to familiarize the reader with the concepts associated with it. The topics will not be discussed in depth; therefore, if the reader desires more detailed coverage of any of the topics, a comprehensive resource would be (Schott, 1997).

2.1.1 Propagation of Energy

In passive optical remote sensing, there are two groups of possible energy paths, namely those originating from a light source such as the sun and those associated with the temperature of objects other than the sun. There are five possible paths that energy can travel when originating from the sun. This concept is illustrated in Figure 2.1-1.

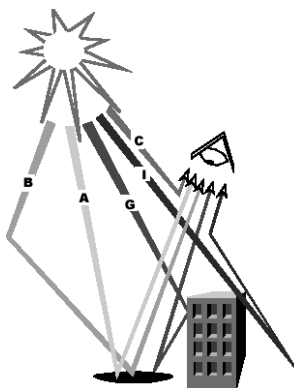


Figure 2.1-1 – Solar Energy Paths (Schott, 1997)

Mathematically, Figure 2.1-1 can be expressed as

$$L_{solar} = L_A + L_B + L_C + L_G + L_I \quad (2.1-1)$$

where

- L_A solar radiance passed through atmosphere, reflected from earth's surface, propagated back through the atmosphere to the sensor
- L_B solar radiance scattered by atmosphere, reflected by earth to the sensor
- L_C solar radiance scattered by the atmosphere directly to the sensor
- L_G solar radiance passed through atmosphere, reflected from background objects, reflected from target back through atmosphere to the sensor
- L_I solar radiance reflected from surrounding objects, scattered into line of sight of sensor (can be lumped with L_C)

The second group of energy paths, those due to self-emission by the target, is illustrated in Figure 2.1-2.

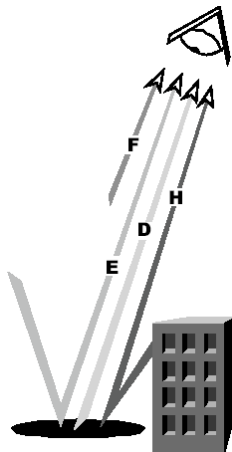


Figure 2.1-2 – Self-emitted thermal energy paths (Schott, 1997)

As with the solar energy paths, the self-emitted thermal energy paths can be mathematically represented as

$$L_{thermal} = L_D + L_E + L_F + L_H \quad (2.1-2)$$

where

L_D self-emitted radiance from target, through the atmosphere to the sensor

L_E self-emitted radiance from the atmosphere, reflected off target through atmosphere to the sensor

L_F self-emitted radiance from atmosphere directly to the sensor

L_H self-emitted radiance from background object, reflected off target through atmosphere to the sensor

By combining the equation for solar energy paths and that for self-emitted thermal energy paths and substituting in the expressions for each of the radiances described in (Schott, 1997), the result is the “Big Equation”

$$L_\lambda = \left\{ E'_{s\lambda} \cos(\sigma) \tau_1(\lambda) \frac{r(\lambda)}{\pi} + \varepsilon(\lambda) L_{T\lambda} + F [E_{ds\lambda} + E_{de\lambda}] \frac{r_d(\lambda)}{\pi} + (1-F) [L_{bs\lambda} + L_{be\lambda}] r_d(\lambda) \right\} \tau_2(\lambda) + L_{us\lambda} + L_{ue\lambda} \quad (2.1-3)$$

where

$E'_{s\lambda}$ exoatmospheric irradiance

σ angle from target normal to the sun (declination angle)

$\tau_1(\lambda)$ transmission through atmosphere along sun-target path

$r(\lambda)$ target reflectance

$\varepsilon(\lambda)$ target emissivity

$L_{T\lambda}$ self-emitted radiance from target at temperature T

F fraction of hemisphere above target that is sky (shape factor)

$1-F$ fraction of hemisphere above target that is background

$E_{ds\lambda}$	downwelled solar irradiance
$E_{de\lambda}$	downwelled self-emitted radiance from atmosphere
$r_d(\lambda)$	target diffuse reflectance
$\tau_2(\lambda)$	transmission through atmosphere along target-sensor path
$L_{bs\lambda}$	background reflected solar radiance onto target
$L_{be\lambda}$	background self-emitted radiance onto target
$L_{us\lambda}$	upwelled solar irradiance
$L_{ue\lambda}$	upwelled self-emitted radiance

The “Big Equation” indicates the sensor-reaching radiance’s dependence on wavelength; therefore, the radiance will change in different parts of the spectrum. This can work to simplify the “Big Equation” because if the imaging is only occurring in the visible or near infrared regions, then the thermal terms can be ignored. Similarly, if the imaging is in the long wave infrared regions, the solar terms can be ignored (Schott, 1997). For the work being done in this thesis, the long wave infrared (IR) bands will not be used in simulating an image; only the electro-optical (EO) bands will be used (approximately 0.4 – 2.5 microns). Therefore, the thermal terms can be ignored for the purposes of this research.

2.1.2 Radiometric Terms

There are many terms that are important in describing the photons originating from the light source and how they interact with the atmosphere and surfaces in the area being imaged. The radiant flux, or power, is a term that describes the rate at which energy is propagating. Similarly, the rate at which the radiant flux is delivered to a surface is called irradiance. Radiant exitance is exactly the same concept as irradiance except that it is the flux per unit area away from the surface rather than onto the surface (Schott, 1997).

Spatial information about the flux is described through the irradiance and exitance while the angular information is described through radiant intensity. This term describes “the flux per unit solid angle from a point source into a particular direction” (Schott, 1997).

Since it requires a few terms to determine both the spatial and angular information, it makes sense to combine these terms into a more comprehensive term. The flux per unit projected area per unit solid angle is defined as the radiance term. Although the most complex of the radiometric terms, it is also the most useful since it provides both spatial and angular information. Most optical images are in terms of radiance values. It is mathematically defined as

$$L = L(x, y, \theta, \phi) = \frac{d^2\Phi}{dA \cos \theta d\Omega} = \frac{dE}{d\Omega \cos \theta} = \frac{dI}{dA \cos \theta} = \frac{dM}{d\Omega \cos \theta} \quad (2.1-4)$$

where

x, y define a spatial location in the plane of interest

θ, ϕ define the angles of the direction of interest relative to the normal of the plane

$d^2\Phi$ second derivative of the radiant flux

dA area element on the surface of interest

$d\Omega$ element of solid angle ($d\Omega = dA/r^2$)

dE first derivative of the irradiance

dI first derivative of the intensity

dM first derivative of the exitance

r radius between two surfaces of interest

Unlike irradiance or exitance, radiance can be used to define the flux onto or away from a surface, as well as through any arbitrary surface in space. Nicodemus demonstrated that radiance is constant over distance along a ray in lossless media. For a more detailed description of his experiment, refer to (Nicodemus, 1976).

It is also important to note that each of the radiometric terms described above is spectrally variable. In other words, each term will vary over wavelength (Schott, 1997).

2.1.3 Electro-Optical Imaging

Many EO camera systems utilize reflective optics, or mirrors, to focus an image onto the focal plane. Although conventional refractive optics (glass lenses) are used as well, they are not as practical for space-based applications due to the heavier weight of the glass lens compared to

the mirror. The desired information in the system is to compute the irradiance onto the focal plane. The detectors in the EO system work to convert the incident flux into electronic signals. At some point, most EO systems convert the signals to digital form and more systems are recording in digital form as well to ease in the transmission of data (Schott, 1997).

These digital signals are then processed in a variety of ways to create the image. Some of the processing involved is correction for geometric distortion, registration of spectral bands, reduction of noise, and radiometric corrections. The final image can either be analyzed digitally or printed out for visual interpretation.

There are several different sensor designs that can be used in EO imaging, including line scanners, whisk-broom imagers, push-broom sensors and framing arrays. The line scanner is perhaps the simplest of the designs because it utilizes a spinning mirror to project an image of the detector onto the ground plane over which the sensor is flying. As the mirror is spinning, the sensor platform is also advancing forward, so that both dimensions are being imaged. One of the problems encountered with line scanners and push brooms is that geometric distortions occur due to the motion of the platform during imaging. This is especially true of airborne sensors since roll, pitch and yaw will all have an effect. Space-based platforms are usually geometrically stabilized, but still encounter distortion due to the motion in the along-track direction. However, there are many techniques that can remove these distortions, so line scanners are still very useful (Schott, 1997).

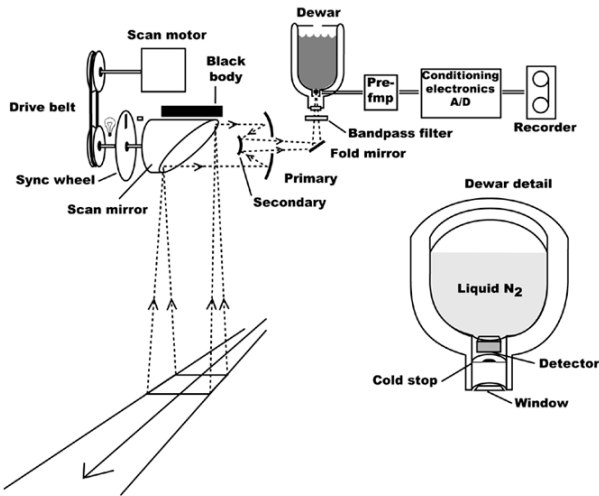


Figure 2.1-3 – Line Scanner design, with liquid nitrogen cooling for thermal bands (Schott, 1997)

For an even longer dwell time, push-broom sensors can be utilized. In this design, the detectors are fashioned in a linear array to collect entire lines of data in one “look”, rather than scanning across a line. A disadvantage to using the linear array is that to achieve a large ground swath, a very long array would be needed. However, with no moving parts, mechanically it is simpler and has a longer expected lifetime than a design with moving parts. Though the spectral bands still need to be registered, the lack of any motion of a scanner reduces the geometric distortions (Schott, 1997).

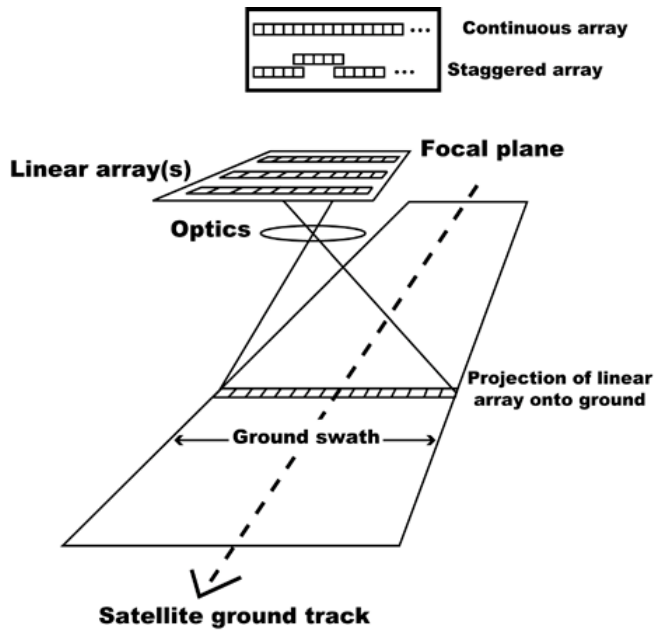


Figure 2.1-4 – Push-broom design (Schott, 1997)

2.2 Radar Fundamentals

This section will give a summary of radar, to include the fundamentals of its operation and the information that can be deduced from the radar returns. It will also delve into the properties of waves that are inherent to radar, such as the Doppler effect. There will also be a discussion on radar imaging and how the energy and backscatter relate to the final imagery.

2.2.1 Basic Radar Concept

Radar, or RAdio Detection and Ranging, transmits electromagnetic energy via antennas into a volume of space in order to search for objects, which will be referred to as targets throughout the document. The energy then reflects off the target and the portion that is directed back towards the radar is used to determine range, angular frequency, velocity, and other target characteristics. Radar most commonly operates in the wavelength range of 1 mm to 1 m. Unlike

optical imaging, which in many cases uses the sun as its energy source, radar systems are active sensors, meaning they use microwave energy to illuminate surface features and record the returned signal (MicroImages, Inc., 2001). Another difference between optical and radar imaging is the ability of microwaves to penetrate all types of atmospheric conditions, including haze, rain, clouds, and smoke, regardless of the available solar illumination (DPI Website, 2004).

The radar antenna acts as both a transmitter and receiver, alternating between the two functions. It sends out a pulse of electromagnetic energy and measures the amount of energy that is backscattered towards the antenna in receive mode. The return is usually weaker than the pulse transmitted since not all the energy was reflected back towards the antenna. The echo is converted to digital data and passed to the data recorder, processed, and displayed. The energy pulse travels at the speed of light, making range calculations rather straightforward since the roundtrip time is known and can be used to calculate the distance of the target from the antenna (NASA JPL, 1996).

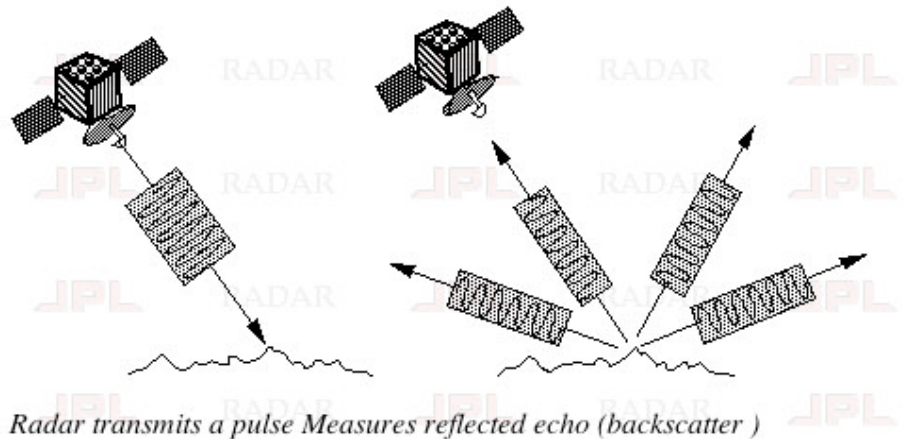


Figure 2.2-1 – Illustration of backscatter (NASA JPL, 1996)

The range of a target can be directly determined using the elapsed time between the transmission of a pulse and the return of the echo. This is the round-trip time, or t ; therefore it is divided in half to determine the time the pulse took to reach the target. The range, R , is then determined by multiplying this time by the speed of light, c .

$$R = \frac{ct}{2} \quad (2.2-1)$$

This technique of measuring range is called pulse delay ranging. It works very accurately as long as the round-trip time for the furthest target is shorter than the time between pulses. However, ambiguities can result when multiple echoes are received before or after the transmission of the next successive pulse. In some cases there is no telling which echoes match up with which transmissions. In the case where the round-trip transit time exceeds the time between pulses, that target will appear much closer than it is in reality (Stimson, 1998).

One way to resolve the ambiguities imposed by this problem is by tagging a pulse with a different frequency, amplitude, or width so that the observer can track the changes in that particular echo in each successive return. The observer can then determine which echo corresponds to a particular pulse and resolve the ambiguity.

Another important concept in radar is the Doppler effect, which is a shift in the frequency of a wave that occurs when an object and its observer (in this case, the radar) are in motion with respect to each other. As the wave approaches the observer, it is compressed, and likewise is expanded when it is moving away from the observer. The effect is greater for higher speeds. Since the relationship between wavelength and frequency is inversely proportional, as the wavelength is shortened, frequency is increased. By sensing the Doppler frequencies, radar can determine range rates as well as discriminate between target echoes and clutter. In the case of ground radar, the only movement relative to the radar is due solely to the target, since the ground has no Doppler shift. Therefore, it is a simple task to differentiate between ground clutter and moving targets. However, with airborne or spaceborne radar, movement could be due to the target as well as to aircraft or spacecraft movement and differentiating between the target and ground clutter becomes a more difficult task (Stimson, 1998).

2.2.2 Real Aperture Radar Imaging

In real aperture radar imaging, the area covered by the airborne or spaceborne radar along its flight path is called the footprint. As the imaging radar moves across the ground along its swath, the data build upon itself to create an image. The resolution is determined by both the

cross-track direction, or range, and by the along-track direction of the image. Range (or cross-track) resolution is determined by bandwidth, whereas in the along-track direction, the resolution is determined by the length of the antenna. The choice of cell size when designing an imaging radar largely depends on the sizes of the targets that will need to be resolved. The amount of signal processing required to produce the images, as well as the cost and the task of interpreting the images are also taken into account. A general rule of thumb when determining the pixel size that will produce useful images is that the required resolution distance should be somewhere between 1/5th and 1/20th the major dimension of the smallest object to be resolved (Stimson, 1998).

The resulting radar image is a series of picture elements, or pixels. Each pixel represents the amount of backscatter received by the antenna for that particular area on the ground. When an object reflects a lot of energy back towards the antenna, the pixel will be bright, whereas a dark pixel or area of the image represents lower backscatter, since less energy was reflected back towards the antenna. Backscatter can also be used to indicate the amount of moisture in the target area, the polarization, the size of the scatterers, and observation angles. Different wavelengths will yield different backscatter as well since material dielectric properties vary with wavelength (NASA JPL, 1996).

The backscatter is also commonly referred to as the radar cross-section (RCS), and is measured in units of area. When the energy from the radar hits a target, it creates electromagnetic energy that radiates in all directions. The target size, orientation, physical shape, and material all determine the amount of energy radiated. These characteristics are lumped together, creating a target's radar cross section (Mahafza, 1998). It is a 1-D representation of how much a target scatters to a far-field sensor, where a large RCS equates to more scattering. Normalized radar cross section, measured in decibels, can be used to remove the dependency on image resolution or pixel size. Typically, the rougher the target, the higher the backscatter, since more energy is likely to be reflected back towards the antenna. Alternately, the smoother the target, the lower the backscatter, since a flat surface will yield more of a specular reflection, resulting in little to no energy scattered back towards the antenna. There does exist a dependency on wavelength as to whether a surface appears rough or not. A surface may appear rough at short wavelengths, but smooth at longer wavelengths (MicroImages, Inc., 2001).

The dielectric constant of objects also plays a role in how it is imaged. For example, metal objects appear bright in radar images because they have high dielectric constants. Generally, the drier the object is, the lower its dielectric constant, and therefore the darker it will appear in the image. However, moisture in soil, vegetation, or snow will increase the dielectric constant and reflectivity (MicroImages, Inc., 2001).

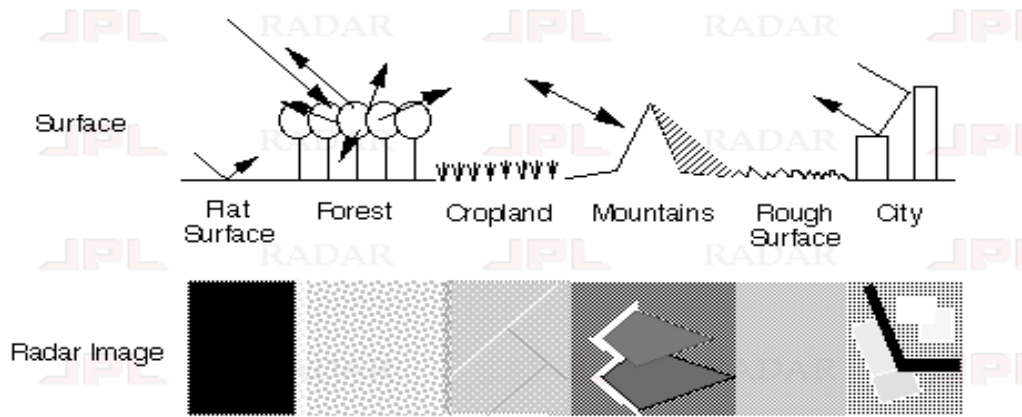


Figure 2.2-2 - Backscatter return for surfaces of different texture (NASA JPL, 1996)

The shape of the object being imaged will also affect its brightness in the radar image. An object that directly faces the sensor, or is perpendicular to the flight path of the sensor, will produce the strongest returns, whereas an object that faces away from the sensor will produce weaker returns. A corner reflector, which results from a 90-degree angle, such as a building intersecting a street, produce the brightest areas since the incoming pulse will double-bounce off the building then the street and reflect directly back towards the antenna (NASA JPL, 1996). This idea is illustrated in Figure 2.2-3. A corner reflector can be used as a means of calibration for the radar.

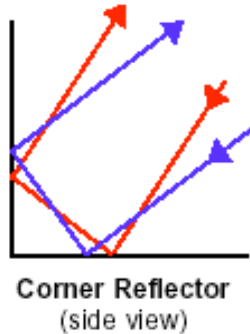


Figure 2.2-3 - Illustration of a corner reflector, such as a building intersecting a street

The amount of energy received from a target depends on three main factors: the radar's average transmitted power, antenna gain, and effective antenna area; the time-on-target; and the target's range and radar cross-section (Stimson, 1998). The general range equation, indicating the energy received from the target during the integration time is

$$\text{Received signal energy} \cong \frac{P_{\text{avg}} G \sigma A_e t_{\text{int}}}{(4\pi)^2 R^4} \quad (2.2-2)$$

where

P_{avg} = average transmitted power

G = antenna gain

σ = radar cross section of target

A_e = effective antenna area

t_{int} = integration time

R = range

This energy, in addition to the noise energy, must exceed a specified threshold in order for the target to be detected. It is usually set just high enough to reduce false alarms to an acceptable rate, where false alarms occur when noise peaks appear as targets.

Any signal received by the radar that is not from the target is considered noise. These signals can come from other objects producing a return or from the thermal effects generated from the receiver, which are impossible to eliminate completely (Mahafza, 1998).

There is always some degree of speckle in radar images, a salt-and-pepper or grainy pattern. A radar system is said to be coherent if there is continuity in the signal phase between one transmitted pulse and the next. Radar waves are coherent in nature, therefore interference, both constructive and destructive, can occur with the radar waves, giving rise to this grainy pattern. There are various image processing techniques that can help reduce the appearance of the graininess, however nothing will completely eliminate it. One method to reduce this effect is by taking multiple images of the same area and averaging the images together to create a smoother product, however it comes at the cost of decreased spatial resolution (JPL AIRSAR website, 2004). The amount of speckle is inversely proportional to the square root of the number of independent images averaged together.

The ability to penetrate subsurface structures with long wavelength signals (>60 cm) is one of the major advantages of radar imaging. Polarimetric radar is able to reveal more information about the composition of the terrain beneath such obscurations as vegetation (Tapley, 2002). A radar system that is not considered polarimetric transmits pulses with a horizontal orientation. Polarimetric radars, also known as dual-polarization radars, transmit pulses with both vertical and horizontal orientations. Since the radar returns are a complicated function of particle size, density, shape and other properties, the additional orientation helps provide more information about the terrain or targets (NSSL website, 2003).

One of the limitations of radar is that no matter how powerful the radar is or how efficient its design, its range is limited to the unobstructed line of sight. It cannot see through such objects as mountains, and it has strong limitations seeing at low altitudes or beyond the horizon when imaging from the ground. Other limitations that can be encountered with radar imaging are obscuration of the return of the echo due to clutter from the ground, certain weather types such as rain, hail or snow depending on the wavelength being used, or jamming by transmissions of other radars (Stimson, 1998). This leads to the signal-to-noise ratio (SNR), which indicates the strength of the returns compared to the strength of the electrical background noise. The greater the SNR, the better chance of detecting a target that gives off weaker echoes, which leads to a greater detection range.

2.3 SAR Fundamentals

This section will introduce the fundamentals of Synthetic Aperture Radar (SAR), to include the basic concept of SAR, resolution, and phase correction.

2.3.1 Basic SAR Concept

SAR is a type of radar capable of achieving finer resolution than conventional means by combining the radar returns from multiple viewing angles. It accomplishes this by keeping track of both the phase and magnitude of each of the returns and combining them in a way that synthesizes a much longer antenna (Richards, 2003).

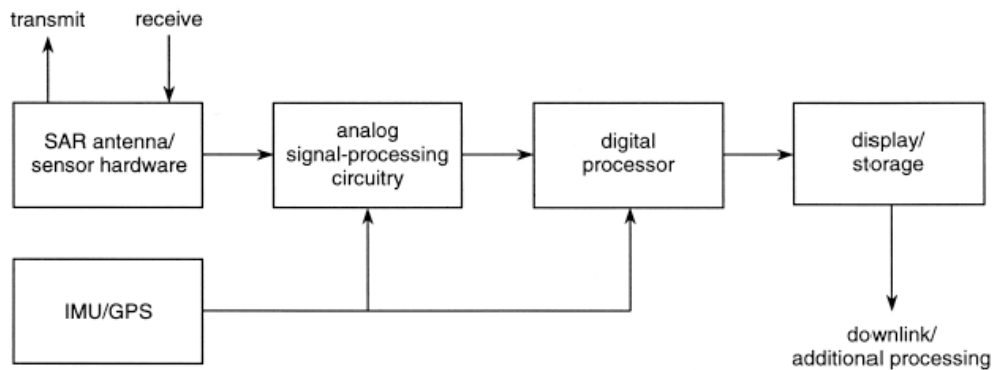


Figure 2.3-1 – Block diagram of a SAR system (Richards, 2003)

SAR utilizes an inertial measurement unit (IMU) and at least one global positioning system (GPS) for sensor motion measurements. These instruments aid in the image formed by the digital processor by helping to coherently combine the multiple returns from the sensor. Both the magnitude and phase of the target's reflectivity density are provided by the SAR system; however, on the display only the magnitude components are usually depicted (Richards, 2003).

Two primary types of SAR imaging exist, stripmap mode and spotlight mode imaging. These are depicted in Figure 2.3-2 and Figure 2.3-3. The first type to be developed was the stripmap mode. It utilizes a sideways-looking antenna that sweeps the ground as the sensor travels along the flight path. In contrast, spotlight mode illuminates the same area on the ground

from every point along its flight path. As a result of the multiple looks at the same fixed spot on the ground, spotlight mode achieves a finer azimuth resolution than stripmap mode; however, the increased resolution is countered by the smaller region imaged as compared to stripmap mode (Richards, 2003). One of the other advantages to spotlight mode is that having the beam continuously trained on a given area helps to reduce the speckle by filling in the gaps in the backscatter (Stimson, 1998).

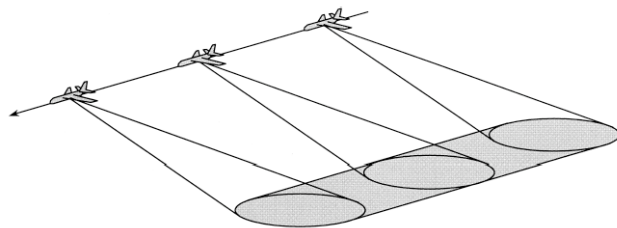


Figure 2.3-2 – Stripmap-mode SAR imaging (Richards, 2003)

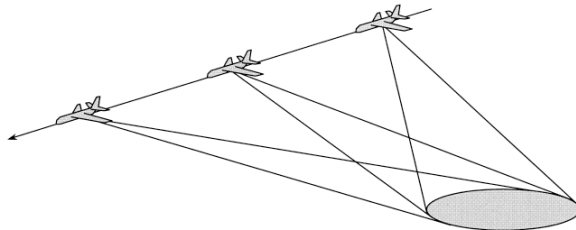


Figure 2.3-3 – Spotlight-mode SAR imaging (Richards, 2003)

There are various other types of SAR imaging as well. The beam of the real antenna can be trained either forward or backward and appropriately focused so that it can map areas that it has long since passed as well as areas it has yet to reach. This is referred to as a squinted array. The drawback is that the effective length of the synthesized array is foreshortened. However, depending on the mission of the system, it might be well worth accepting the foreshortening in exchange for versatility in mapping areas.

Multilook mapping is the name given to a radar who's real antenna is wide enough to enable mapping of an area several times without the need for changing the radar's look angle. Many radar images are the result of more than one look at an area.

2.3.2 Sidelobes

Besides the main lobe of a radar return, weaker sidelobes are produced alongside the main lobe as shown in Figure 2.3-4. If the antenna is significantly larger than the wavelength of the transmitted signal, the beam is much more focused and the sidelobes are almost undetectable, however a large enough antenna is usually not practical to completely rid the signal of sidelobes. The sidelobes do not extend a large distance and have weak power densities, however they can still show up in the radar image. The further out from the main beam the sidelobe resides, the weaker the power density. Stronger sidelobes may result in weak or false targets appearing next to strong targets. The combined sidelobe return from all targets may degrade detail in the image (Stimson, 1998). Large sidelobes may also lead to multiple images of a single target in the radar image.

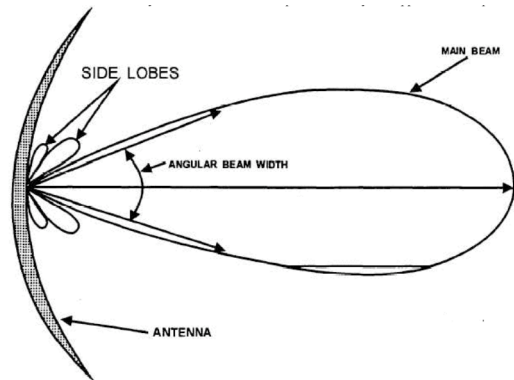


Figure 2.3-4 – Radar beam sidelobes (Integrated Publishing, 2004)

2.3.3 Resolution

The range resolution (or cross-track resolution) is improved by increasing the bandwidth. In practice, however, there is a limit to the finest resolution attainable due to certain physical and operational considerations.

Compared to conventional radar, SAR is able to obtain much finer resolution in the azimuth, or line of flight, direction since it is synthesizing a much larger aperture. The azimuth resolution is determined by the width of the antenna beam – the narrower the beamwidth, the

better the resolution. However, for a beamwidth to be narrow, the antenna must be long. Equations 2.3-1 and 2.3-2 describe the azimuth resolution and beamwidth for a real antenna:

$$\text{Real Beamwidth: } \beta_A = \frac{\lambda}{D} \quad (2.3-1)$$

$$\text{Real Resolution: } \Delta L = \beta R = L_s \text{ (synthetic aperture length)} \quad (2.3-2)$$

where λ is the wavelength, D is the aperture of the radar, and R is the slant range (PROFC, 2005). Equation 2.3-2 is depicting how, in the azimuth direction, the beamwidth by range projected for the synthetic aperture of a certain length is the same as for a real aperture radar of the same length.

Antenna length can present problems on airborne and spaceborne sensors, therefore a different approach must be taken. SAR systems utilize a short antenna, however they synthesize the effect of a long antenna (Lillesand et al, 1994). This results in not only a longer effective antenna, but also a much narrower beamwidth, even at long ranges, but without requiring short operating wavelengths. In short, SAR synthesizes a very long antenna by combining the multiple returns from a shorter antenna. Equations 2.3-3 and 2.3-4 describe the beamwidth and resolution for a SAR antenna.

$$\text{Synthetic Beamwidth: } \beta_s = \frac{\lambda}{2L_s} = \frac{D}{2R} \quad (2.3-3)$$

$$\text{Synthetic Resolution: } \Delta L_s = \beta_s R = \frac{D}{2} \quad (2.3-4)$$

Notice that the resolution is no longer dependent on range, which explains why SAR systems have a high resolution regardless of the slant range or high altitude of the system (PROFC, 2005).

2.3.4 Phase Correction

The distances from the radar to the target will be slightly different for each return. These differences can result in differences in the phases of the returns. In a system that does not account for the phase differences, the resulting image will appear unfocused; therefore this type of system is an unfocused array. By applying an appropriate phase correction to the returns

received from each array element, the system becomes a focused array. The phase correction is calculated as

$$\text{Phase correction} = -\frac{2\pi}{\lambda R} d_n^2 \quad (2.3-5)$$

where

d_n distance of element n from array center

λ wavelength (same units as d_n)

R range to area being mapped (same units as λ)

To reduce computation time, in some cases it is possible to sum the returns of a few adjacent elements and perform the phase corrections on the sums rather than all of the individual returns. This type of phase correction is a line-by-line correction, and in and of itself can present long computation times, even if pre-summing is done to reduce the number of phase corrections needed. However, Doppler processing helps reduce this computation time. In Doppler processing, a phase correction converts the return from each point on the ground to a constant frequency. That frequency corresponds to the azimuth angle of the point on the ground from which the return was received. These frequencies will be relatively constant over the integration time (the length of time the aircraft or spacecraft takes to fly the array length) and they are relatively evenly spaced. Therefore, the filters can be formed using the Fast Fourier Transform (FFT) (Stimson, 1998).

The filters are formed at the end of the integration period and therefore can be treated as a block and transferred to the proper positions on the display. While this is occurring, the radar has moved another array length and accumulated similar data and will repeat the process over again. Using the Doppler processing method requires only one phase rotation for each range bin and therefore is much faster in processing time than the line-by-line method. In fact, for the line-by-line processing, the number of phase rotations needed is N^2 (where N is the number of pulses integrated). In Doppler processing, the number of phase rotations needed is $N(1+0.5\log_2 N)$.

A simple example will be presented to illustrate the number of computations this represents. Suppose a synthetic array has 1024 elements. For line-by-line processing, this results in 1024^2 , or 1,048,576, phase rotations. In Doppler processing, the number of phase rotations

needed would be $1024(1+0.5\log_2 1024)$, or 6,144. That is approximately 170 times less than line-by-line processing. For a more detailed discussion on the mathematics behind Doppler processing, the reader should refer to (Stimson, 1998) or a similar resource discussing SAR fundamentals.

Uncompensated phase errors can result in significant spreading of the synthetic beam, resulting in serious degradation of the resolution of the image, reduced antenna peak gain, beam wander, and increased sidelobe errors. Some of the common sources of phase errors are: unmeasured velocity error, unmeasured acceleration along the line of sight, non-linear motion of the platform, equipment imperfections, processing approximations, and atmospheric disturbances (Stimson, 1998).

2.3.5 Motion Compensation

As mentioned in the phase correction section, slight differences in distances to the target can result in differing phases. For this reason, it is important to correct for any extraneous motion in the platform carrying the radar system so that it does not interfere with the phase correction. The acceleration of the platform can be measured using accelerometers or by an inertial navigation system (INS). Once the acceleration is measured, the phase corrections are computed and applied to the signals.

2.3.6 Signal Phase Equation

Though there are various ways to represent the signal phase equation that comprises a SAR image, the fundamentals are all very similar. This section will use the equations laid out in (Carrara et al, 1995) to detail the SAR image formation equations. The first step in image generation is for the SAR system to generate and transmit a pulse. The pulse is in the form of a linear frequency modulated (FM) chirp signal, represented by Equation 2.3-6.

$$s_t(n, t) = A(t) \cos[2\pi f_c t + \pi\gamma(t - nT)^2] \quad (2.3-6)$$

where

γ	chirp rate
T	interpulse period
f_c	center frequency
n	pulse number
$t - nT$	fast time (time within a signal received from a specific transmitted pulse)

Since Equation 2.3-6 is in a continuous form, it is reasonable to choose a rectangular pulse shape and to represent the real signal in complex exponential form. Therefore, the more accurate transmitted signal becomes what is shown in Equation 2.3-7.

$$s_x(n, t) = A_0 \text{rect}\left(\frac{\hat{t}}{T_p}\right) e^{j[2\pi f_c t + \pi\gamma t^2]} \quad (2.3-7)$$

where

A_0	amplitude
\hat{t}	$t - nT$
T_p	transmitted pulse length

and the definition of the *rect()* function is

$$\text{rect}(u) = \begin{cases} 1, & |u| \leq \frac{1}{2} \\ 0, & |u| > \frac{1}{2} \end{cases} \quad (2.3-8)$$

Assuming an ideal point scatterer with amplitude and phase characteristics that do not vary with frequency and aspect angle, the signal received from a single point target at pulse n is depicted in Equation 2.3-9.

$$s_r(n, t) = a_r \operatorname{rect}\left(\frac{\hat{t} - t_d}{T_p}\right) e^{j2\pi f_c(t-t_d)} e^{j\pi\gamma(\hat{t}-t_d)^2} \quad (2.3-9)$$

where

σ_t radar cross section of point target

$a_t = \sqrt{\sigma_t}$

t_d total time delay from transmit antenna to target and back to receive antenna

The previous equations for the transmitted and received signals describe the signals for point targets in the interest of simplicity and ignore any attenuation due to the propagation of the signal between the radar system and the scene. They also ignore any antenna gain, amplitude effects and time delays from atmospheric effects. Figure 2.3-5 is a block diagram that illustrates how the transmitted and received signals eventually form a SAR image.

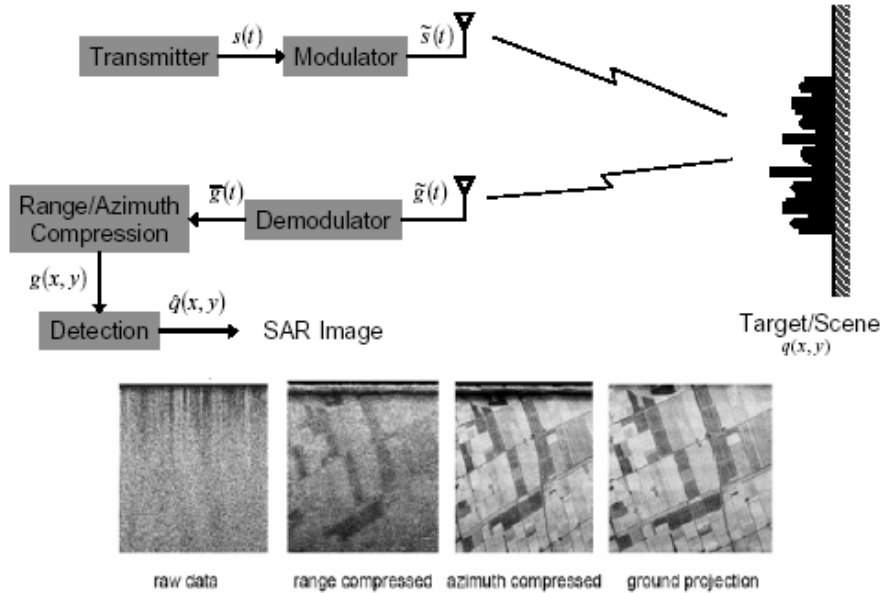


Figure 2.3-5 – SAR image formation block diagram (Blevins, 2004)

2.4 DIRSIG

Digital Imaging and Remote Sensing Image Generation, or DIRSIG, is a synthetic image generation tool developed in the Digital Imaging and Remote Sensing (DIRS) Laboratory at Rochester Institute of Technology (RIT). The tool was designed to model broadband, multi-spectral and hyper-spectral imagery using principles such as bi-directional reflectance distribution function (BRDF) predictions and the geometry of a line scanner. Using programs such as MODTRAN and FASCODE, images can be simulated that are radiometrically accurate for a user-defined number of bandpasses (DIRSIG Manual, 2004).

One of the main goals in the development of DIRSIG was to create a tool that could accurately generate comparable real-world imagery from a variety of sensors for use in testing various algorithms. Since the cost of performing live data collects with actual sensors for the purposes of testing algorithms is so high, tools such as DIRSIG can help accomplish the same end result at a significant cost savings. The resulting images from DIRSIG are capable of representing mixed pixels, different illumination conditions, and real-world spectral characteristics using first principles-based approaches. Theories fundamental to chemistry, physics and mathematics were used to predict such things as the interactions between light and matter, the behavior of photons with various materials, and surface temperatures based on conductivity, density, convective loadings, etc (DIRSIG Manual, 2004). It should be noted that simulated imagery is only a cost-effective tool to test algorithms and should not be used to completely replace the use of actual imagery for validation.

An enhanced CAD environment is used to generate every object in a scene in DIRSIG. Constructing a scene is a difficult process. First, the area to be modeled must be chosen. It is best to choose an area for which ground truth is available so as to make the model as accurate as possible. The next step is to generate or locate terrain data for the area, which could be in the form of a Digital Elevation Model (DEM). Upon generating the terrain data, or locating a DEM to be used, the model of the terrain has to be constructed. Following this, 3-D models of all the objects in the scene need to be constructed in the CAD environment. Once the drawing is made, each object is facetized, which involves using two-dimensional polygons to create 3-dimensional objects. This process can result in hundreds of thousands of individual facets for very detailed

objects. Using a program called Bulldozer that is part of DIRSIG, each facet is assigned optical and thermodynamic properties that represent the material of the facet. A DIRSIG material database must be created, or an existing database can be used from a similar scene. Using the Bulldozer tool in DIRSIG, the CAD objects need to be imported and attributed, and saved as a Geometric Database File. The Bulldozer tool is also used to place the attributed objects onto the terrain. When all these steps are accomplished, a configuration file is created to simulate a sensor that will image the scene and the simulation is run (DIRSIG Manual, 2004).

DIRSIG tries to accurately model scenes through various approaches that model real-world occurrences. MODTRAN is an atmospheric radiative transfer code used to predict path transmissions and radiances within the atmosphere (DIRSIG Manual, 2004). FASCODE is similar to MODTRAN, however it works as a line-by-line model rather than a band model, as MODTRAN does (DIRSIG Manual, 2004). It is also useful for finer spectral resolution modeling than MODTRAN. However, it does not include the scattering support of MODTRAN, therefore modeling at shorter wavelengths can be affected. Other factors taken into consideration in DIRSIG are the effects of neighboring objects on each other, path geometry, atmospheric scattering, downwelled and upwelled radiances, and path length.

A passive thermodynamic model called THERM is used in DIRSIG for temperature prediction. When modeling in the thermal region of the spectrum, the temperature of targets and their backgrounds play an important role in the target's signature. THERM uses meteorological characteristics such as wind speed, humidity, and air temperature to model temperatures. Using the THERM model, DIRSIG is able to accurately model thermal inertia of various environmentally heated objects. However, as mentioned in the Optical Radiation Propagation section, the thermal bands will not be modeled in this research, therefore THERM will not play a role in the DIRSIG modeling of the chosen scenes.

Spatial variations in reflectance account for the appearance of texture in real imagery. Therefore, DIRSIG utilizes a database of reflectance curves for each of the materials in the simulated imagery to model the appearance of texture. DIRSIG also uses bi-directional reflectance models to account for variances due to orientation and surface structure (DIRSIG Manual, 2004). Surface temperature affects the texture in the thermal region, and this is

accounted for by modeling the solar absorption and thermal emissivity through a convolution with a blackbody distribution (DIRSIG Manual, 2004).

DIRSIG is based on a ray tracing approach to correctly account for geometric effects on the incident and emitted radiation in the model at each facet of an object. A ray (or multiple rays in the oversampled case) is cast into the scene from each pixel at the focal plane of the sensor and each interaction the ray encounters is recorded. The recorded ray is then cast at the sun to determine the proper solar shadowing for the specified time of day, and any solar loading for up to 24 hours previous are taken into account. The ray tracing approach is illustrated in Figure 2.4-1. Rays are also cast from the facet to the hemisphere above the target to account for the downwelled radiance received by the target. A BRDF model can be assigned for each material in a scene. DIRSIG utilizes approximately 100 rays that are simultaneously cast into the hemisphere to include radiances from both sky and background sources. These radiances are correctly weighted by each of their respective reflectances (DIRSIG Manual, 2004).

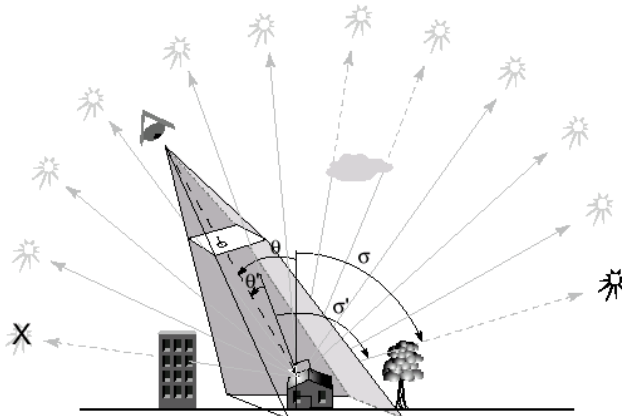


Figure 2.4-1 – DIRSIG ray tracing (Peterson, 2004)

A variety of sensors can be modeled in DIRSIG, to include line scanners, pushbrooms, and whiskbrooms. Mixed pixels can be simulated and the model incorporates many of the challenges that a user would actually encounter in obtaining actual imagery. Although the end result will be an “ideal” image, there are post-processing tools in DIRSIG that allow the user to account for varying MTF (modulation transfer functions) and noise (DIRSIG Manual, 2004).

The interaction among all the submodels of DIRSIG can be illustrated in the flowchart in Figure 2.4-2.

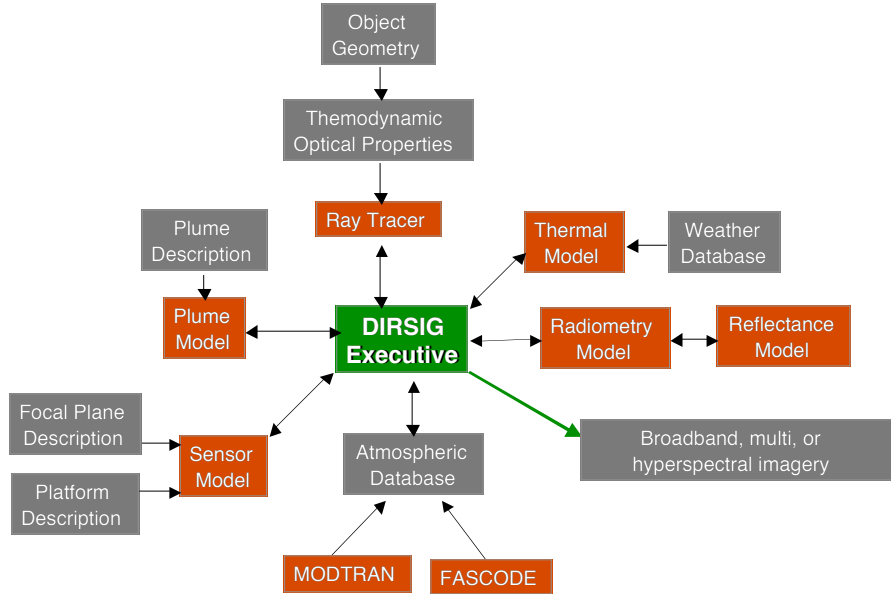


Figure 2.4-2 – DIRSIG submodel interactions (Peterson, 2004)

There are other EO simulation tools available as well. One such signature prediction code is GTSIG (Georgia Tech Signature Model). It has the ability to include effects of clutter from both real and synthetic terrain as well as predicting propagation path models. It uses the object's surface geometry, optical properties, and a thermal network to describe the internal structure. GTSIG is also capable of predicting radiance and background temperatures (Georgia Tech Research Institute, 2004).

CameoSim is another software package capable of generating synthetic EO imagery. It is a physics-based program that produces radiometrically accurate imagery. The user has the ability to control time of day, time of year, weather conditions and other such properties. CameoSim is also capable of accurately modeling atmospheric effects on the scene (Sutherland et al, 2004).

DIRSIG is a robust EO/IR simulation tool that is widely used in the community and already available at RIT. It also has many similarities to Xpatch, the radar simulation tool that will be used in this research. Therefore, DIRSIG will be the tool used to accomplish the EO scene generation for the purposes of this thesis.

2.5 Xpatch

This section will introduce a radar simulation tool called Xpatch, developed by DEMACO/SAIC (SAIC website, 2001). The section will begin with an overview of the basic principles that underlie the way in which Xpatch runs, to include the approximations and limitations of the tool. A discussion will follow of the two tools within Xpatch developed by the Advanced Technology Applications division of SAIC. These tools are ModelMan and Pioneer and are powerful pre- and post-processing Xpatch tools.

2.5.1 Xpatch Overview

Xpatch is similar to DIRSIG, in that it is a simulation tool, the difference being that it is for simulating radar imaging, rather than EO/IR imaging. Objects are represented in a computer-aided design (CAD) format and Xpatch is used to predict their radar signature and high frequency electromagnetic scattering. The tool was developed by DEMACO (purchased by SAIC in 1998) under the tri-Service sponsorship of Wright Laboratory at Wright-Patterson AFB , Phillips Laboratory at Kirtland AFB, the Army Research Laboratory at Ft. Belvoir, and the Naval Air Warfare Center at Pt. Mugu.

Xpatch was originally developed to prevent “friendly fire” incidents in military operations, where a warfighter mistakenly fires upon their own aircraft, tank or ship. The responsibility of Xpatch was to determine friend and foe by analyzing the radar signature of a military vehicle and predicting its identity (SAIC website, 2001).

The Xpatch tool is an approximate solver and does not produce answers exact to actual scattering theory. The basic premise behind Xpatch’s capability for radar image simulation is to calculate the polarimetric return from complex geometries of objects in a CAD format using the high frequency shooting and bouncing ray (SBR) technique. In calculating the ray geometry, the most time-consuming aspect is the first bounce, since shadows and blockage checks must be performed. After this occurs, Physical Optics (PO) is used to determine the contribution of the first bounce (Andersh et al, 1994).

Similar to DIRSIG, millions of parallel rays are projected toward the object to calculate the multiple-bounce effects. Each ray is traced by geometric optics (GO), taking into account

reflection coefficients, polarization, and ray divergence, and all the rays are then summed to determine the final scattered field. At the last hit point, PO is used to do the integration. Edge diffraction is an option that can be considered as well, depending on the geometry of the object being imaged. Although only metal edges, specifically PEC (perfect electric conductors), can be modeled with edge diffraction. Seventy percent of the computation time in Xpatch is spent on ray tracing.

In setting up the input file to run Xpatch, the user must choose the method by which to compute the first bounce off the object. The choices are PO, Z-buffer, and SBR. PO is the most accurate way in which to calculate the first bounce effects, however it is also the most time consuming because in this method rays are shot backwards towards the incident plane to determine if there is blockage, indicating whether or not that area of the geometry would contribute to the overall scattering.

Z-buffer is extremely fast compared to PO, however the trade-off is accuracy. It works by using a grid system to determine what objects are blocked and which ones will contribute to scattering, however it is not as accurate as shooting the rays backwards towards the incident field as in PO. SBR is slightly slower than Z-buffer but results in approximately the same accuracy. SBR and PO can be used for all CAD geometries, while Z-buffer is for facets only.

To cut down on computation time, a technique has been developed in Xpatch that allows surface curvature to be modeled as a flat-faceted geometry. However, this requires a larger core memory because more facets are needed to describe an object than if it was modeled as a curved surface. For curved surfaces, approximately ten facets per wavelength of the radar system would be needed to describe a curved surface using facets. IGES (Initial Graphics Exchange Specification) formats should be used to model curved surfaces whenever possible since they will produce a more accurate return from the tool (Xpatch Training, 2004). An object can be represented in Xpatch by both facets and IGES formats as long as they are specified in two separate input files. For example, as illustrated in Figure 2.5-1, if a curved surface were 3 cm in length and the wavelength being used to image the surface was 3 cm as well, the surface would need to be comprised of at least 10 facets to be imaged with any amount of fidelity. Each of the triangles represents a facet. This figure is only meant to illustrate to the reader the concept of the

number of facets needed to describe the curved surface for Xpatch imaging and is not meant to replicate an actual image or its facets.

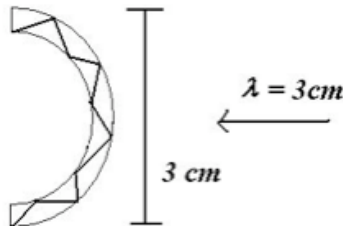


Figure 2.5-1 – Illustration of facet requirement for curved surfaces

Xpatch is used to predict four kinds of radar signatures: RCS, Range Profile, SAR Image, and Scattering Centers. RCS is a 1-D representation, SAR a 2-D, and Scattering Centers a 3-D representation. Xpatch describes RCS in terms of polarization. The outputs the user will obtain when running Xpatch to output an RCS is a list of four polarizations (VV, HH, VH, HV) for each of the frequencies and look angles that were input into the model. The format of the polarizations is such that the first letter is the resulting polarization scattering and the second letter is the incident polarization. For example, HV would be horizontal polarization scattering due to vertical polarization incidence.

When Xpatch is instructed to output the range profile for a target, it outputs a 1-D representation, depicting the returns as a function of time along the length of the target. A single look angle and sweeping frequency are the necessary user inputs to obtain a range profile. The user should be sure to “look” far enough past the target in a range profile to ensure that all multiple-bounce effects are modeled. For example, if the target is an aircraft with inlets, one or more of the rays could experience many bounces through the length of the inlet, and since these bounces would take more time than a single bounce, they will appear further along the time axis of the range profile, appearing after the end of the target. This is because a longer pathlength will appear as if it is further away than it actually is.

A SAR image presents a clear physical picture of the scattering, since it is represented in 2-D. Radar scattering from real targets is a vector sum and is sensitive to small changes in the

target and environment. A SAR image gives the phase history data of a target in both the cross range and along-track directions.

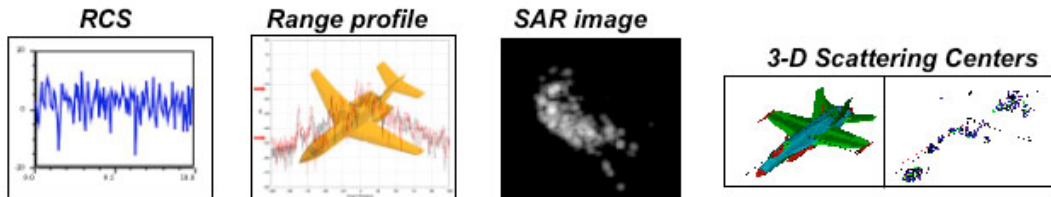


Figure 2.5-2 – Xpatch outputs (SAIC, 2004)

The first step in using Xpatch is to give it a geometrical input of an object, which would be represented in CAD as either a faceted model or an IGES model. This is the most difficult step, both for Xpatch and DIRSIG simulations, because the user has to know where the objects surfaces are and what those surfaces are made of material-wise. The CAD representation must be as close to real life as possible since any difference in angle or material will result in a different return than the real object would produce for a given radar system.

Xpatch is a high frequency model that uses the physical theory of diffraction (PTD), geometrical theory of diffraction (GTD) and the shooting and bouncing ray technique (SBR), which implements both GTD and PTD. These are all approximations of Maxwell's Equations, and therefore will give an approximate solution. Xpatch also has the capability of producing exact solutions, using full wave theory, such as MoM (method of moments), FEM (finite element moments), and FDTD (finite difference time domain). However, these are all very computationally intensive and in some cases could take months or even years to solve exactly. Therefore, the approximate solutions are a more attractive method. It should be noted that the approximate solutions are only valid in Xpatch for electrically large objects ($\sim 10\lambda$ or larger). Leaves of a tree, for example, would not produce accurate returns in Xpatch unless the frequency was extremely high, which would result in very small wavelengths. X-band radar modeling, which operates at a frequency of about 10 Ghz, would produce wavelengths of about one inch. Leaves are generally not 10 inches or larger, and therefore would not be modeled correctly in Xpatch.

Table 2.5-1 shows a few example frequencies to give the reader an idea of how electrically large an object would need to be in order to be modeled in the various frequency bands correctly. For small objects, such as the leaves mentioned above, Xpatch can be used without producing completely erroneous results, but the results should be noted to be less accurate than for electrically large objects. Therefore, when comparing the simulated data to measured data, the difficulty Xpatch experiences in modeling electrically small objects can account for any differences between the datasets.

Band	Frequency (GHz)	Wavelength (λ) cm	Smallest Object Accurately Modeled (10λ) cm
Ka	38	0.8	8
Ku	15	2	20
X	10	3	30
C	6	5	50
S	3	10	100

Table 2.5-1 - Example Radar Frequencies with Object Sizes

One of the limitations of Xpatch is that it does not account for the effects of motion; i.e. the Doppler effect is not accounted for in the calculations. It also does not consider sensor characteristics or motion. Another thing to keep in mind with Xpatch is that when modeling edge diffraction, not only does it have to be a PEC edge, but Xpatch does not have the ability to extract edges from IGES models. The IGES model needs to be converted to a facet model, after which the edges can be extracted. The next release of Xpatch will have the ability to support material edges other than PEC, however at this time, regardless of the material of the edge, Xpatch will treat it as PEC and the results for the edges will be invalid.

Another limitation of Xpatch has to do with polarizations. The cross-pole RCS values (HV and VH) have not been fully validated in Xpatch. Therefore, although Xpatch outputs will include values for HV and VH, they may not be extremely accurate so it is better to use only the co-pole values (VV and HH) whenever possible. The current version of Xpatch also does not perform calculations on some of the higher order scattering effects such as creeping waves or traveling waves.

2.5.2 Pre- and Post-Processing Tools

The graphical users interface (GUI) of Xpatch is actually a compilation of multiple pre- and post-processing tools that the user may employ on the data. These analysis tools are: cifer, XEdge, xyplot, McImage and XSignal. Cifer is a translation tool that allows the user to convert one type of CAD format into another. It also has the capability of transforming an IGES model into a facetized one as well as texturizing existing geometries to make a ground plane behave more like grass, for example.

The XEdge tool allows the user to view the CAD geometry from any angle, as a solid geometry or a wireframe. The wireframe option depicts all the facets of the object, if it is a facetized model. The user can also shoot multiple rays at the geometry from a specified look angle to determine if the bounces seem reasonable, which will help the user to determine if there are errors in the CAD model.

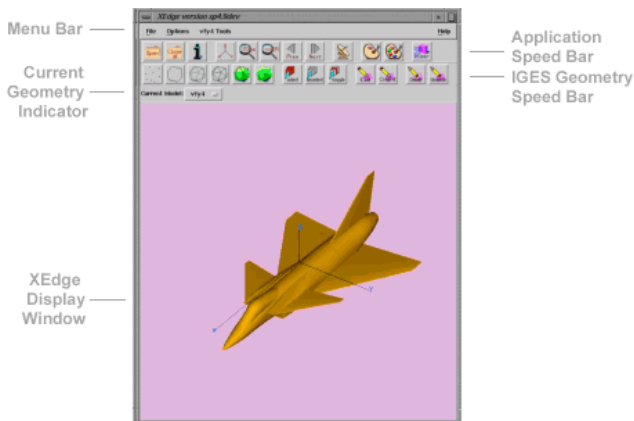


Figure 2.5-3 – XEdge GUI (SAIC, 2004)

Xyplot is a post-processing tool used to model the resulting data in the form of x-y plots. Some of the options included in this tool are the ability to depict multiple data sets on one plot as well as view the data list, in the form of an ASCII file format. One of the drawbacks of xyplot is the resulting plots cannot be saved as a common image format, such as JPEG. The user would have to do a screen shot and convert it using some other program. However, as will be discussed in one of the next sections, there is another tool called Pioneer, which affords the user the ability to save plots as any number of common image formats, such as JPEG.

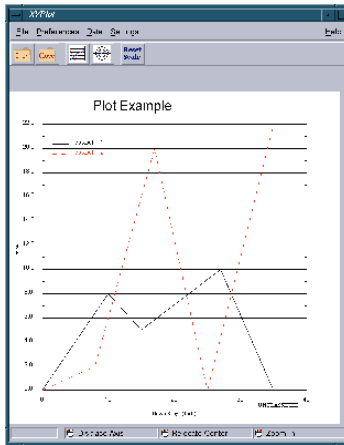


Figure 2.5-4 – Xyplot display window (SAIC, 2004)

McImage is used to display the CAD file along with the measured and predicted time domain signatures to view the effects of scattering. McImage is useful in that it allows the user to overlay the CAD geometry on the resulting plots so that the cause and effect of scattering are more easily visualized. It is also the tool used for displaying resulting SAR images, as shown in Figure 2.5-5.

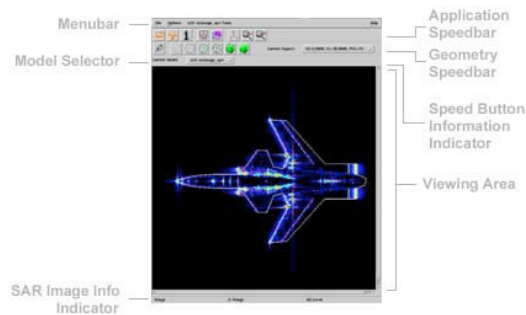


Figure 2.5-5 – McImage display window (SAIC, 2004)

XSignal is a tool used to calculate and evaluate resulting signatures from the Xpatch simulation. It allows for the comparison of RCS, range profiles and SAR imagery. Once the signatures are added to XSignal the user then defines the error metric that will be used to compute the error of the signatures.

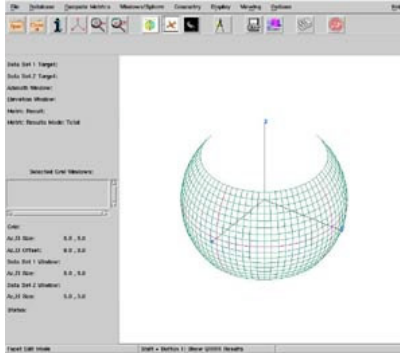


Figure 2.5-6 – XSignal display window (SAIC, 2004)

2.5.3 ModelMan

ModelMan is a tool within Xpatch, developed by the Advanced Technology Applications division of SAIC in Huntsville, AL. Some of the capabilities in ModelMan can be done elsewhere in Xpatch, however ModelMan encompasses these capabilities all in one place and in some instances makes manipulating the geometries easier.



Figure 2.5-7 – ModelMan display window (SAIC, 2004)

One of the most basic capabilities of ModelMan is to read and write facet geometries as well as to organize facets or groups of facets into a visual tree. This grouping allows the user to manipulate many facets grouped as one in a variety of ways. For example, if the geometry is a military tank, the user can group the facets that comprise the turret into one group and manipulate

the turret as a whole. ModelMan allows the user to articulate these groups as well. The turret could be articulated to be modeled at many different azimuth and elevation angles.

Another capability of ModelMan is to allow the user to view parts of the geometry that are normally hidden from normal view. In the same example of the military tank, the wheels could be removed so as to view the geometry behind the wheels to determine the effect this geometry will have on the returns after being run through Xpatch.

Material properties can also be defined for the various facets in a geometry using ModelMan. Edge extraction is another capability of ModelMan for the purposes of obtaining accurate radar returns when edge effects must be considered. Both of these capabilities are available in other parts of Xpatch, however it is convenient to be able to manipulate both of these in the same part of the tool, and the edge extraction tool is somewhat more intuitive in ModelMan.

Another option, called level of resolution (LOR), allows the user to decrease the resolution of a certain part of the geometry. For example, in the turret on the tank, if the user wishes to decrease the current resolution so that the computation time is faster, using the LOR option would decrease the number of facets used to approximate the curvature in the turret. ModelMan allows the user to choose which LOR to use if multiple LORs have been created; therefore, none of the previous LORs are lost when the user decides to decrease the resolution.

2.5.4 Pioneer

The tool called Pioneer within Xpatch is another capability developed by the Advanced Technology Applications division of SAIC. Pioneer is a powerful post-processing tool used for data visualization and comparison of synthetic and measured data.

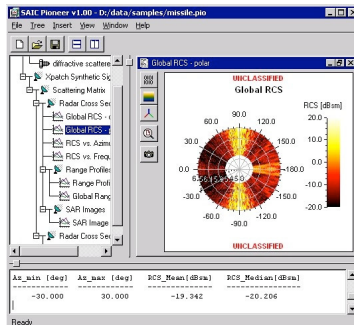


Figure 2.5-8 – Pioneer display window (SAIC, 2004)

Pioneer allows the user to import data files from various sources such as Xpatch, measured data sources, or even Pioneer itself. The user drags and drops the file type into the main window and creates a wiring diagram connecting sources to filters and eventually to a viewer, which allows the user to visualize the data. The wiring diagram allows the user to link data from various sources and display them on the same graph. This is extremely useful for comparing measured and synthetic data.

The outputs of Pioneer can be a variety of graphs, to include X-Y plots, image plots, and 3-D geometry viewing. These can all be saved as JPEG or other format for use in other applications. There is also multimedia capability within Pioneer so the user can record an MPEG or AVI format movie of Pioneer cycling through a graph at sweeping frequencies, for example.

There are a number of radar simulation tools other than Xpatch. EMSARS (Electromagnetic Model of Scattering Applied to Remote Sensing) is a software package developed by Yang et al (1994). It uses first-principle scattering and incorporates both volume scattering and surface scattering effects. The input it uses is the GIS (Geographic Information System) database, which includes terrain features, elevation maps, shadowing, and other detailed ground truth information. A company called Vexcel has developed a product called Scatter, a Phase History Simulator. It has the ability to simulate phase history raw data for a space-based SAR system. The raw data can then be fed into a number of their other programs for processing. It can simulate stripmap, scan mode, or interferometric data (Vexcel website, 2004). Though both of these products, as well as the variety of other radar simulation packages that exist, are viable options for simulating the data that will be used in this research, Xpatch has been used by

some RIT staff and therefore was an available starting point. At this point in time, the research of combining radar and HSI simulated data is more of a feasibility demonstration and therefore it is not critical to decide which tool works best with the data.

3 Experimental Design

This section will begin with a description of the YOGI experiment, which is the basis of the synthetic scenes modeled in both DIRSIG and Xpatch. Included in this description will be specific information about the objects chosen to be imaged in the tools. A subsequent description will follow detailing the approach used to develop the synthetic data in DIRSIG and Xpatch.

3.1 YOGI Experiment

YOGI (Yellowstone Optical and SAR Ground Imaging) is the dataset associated with a multi-agency data collection effort for an area just outside of Yellowstone National Park. Analysis is funded by AFRL/SN (Air Force Research Laboratory/Sensors) under RASER (Revolutionary Automatic Target Recognition and SEnsor Research). RASER is a program through which AFRL supports research efforts. RIT is one organization under RASER receiving money to analyze the YOGI data. These data are available to support a statement of work entitled “Mathematical Modeling and Fusion of Hyperspectral and Synthetic Aperture Radar Data in Open and Urban Landscapes.” The work is a funded effort and will attempt to generate synthetic imagery for the area and combine the SAR and hyperspectral data into a fused image.

The organizations involved in this data collection effort included the Naval Research Laboratory (NRL) Optical Sciences Division, MIT Lincoln Laboratory, Defense Advanced Research Projects Agency (DARPA) Information Exploitation Office, HyPerspectives/Yellowstone Ecological Research Center, JPSD Rapid Terrain Visualization Program, Air Force Research Laboratory, U.S. Forest Service and Yellowstone National Park. The data collection occurred in the summer of 2003, involving a multitude of sensors. Some of the objectives of the data collection were: development and assessment of a terrain characterization algorithm, development of a change detection algorithm, and modeling of terrain height (Orloff et al, March 2004).

Each of the organizations involved in the YOGI experiment had their own roles and objectives in the effort. The Naval Research Laboratory wanted coincident HSI, EO/IR, SAR and LIDAR data for a common geographical area. This would assist in improving target detection

methods and terrain characterization by fusing the various datasets. They were also interested in supporting efforts to improve anomaly detection, matched filtering, and change detection algorithms for HSI data. The data collected in the YOGI experiment would also assist in evaluating the detection performance of various HSI and SAR detection algorithms as well as fusion detection algorithms. Furthermore, the data could be used to support scene classification algorithms for terrain characterization and trafficability (Orloff et al, March 2004).

MIT Lincoln Laboratory's efforts as part of the YOGI experiment were supported by the Deputy Undersecretary of Defense for Science and Technology (DUSD (S&T)) through the Hyperspectral Technology Assessment Program (HTAP), as well as by DARPA/IXO Terrain Characterization Program. MIT Lincoln Laboratory produced a dataset for the multiple sensors for use in algorithm development and terrain characterization. In addition to the multisensor dataset, they included extensive ground truth measurements, such as landcover, vegetation and soil characteristics, and photos (Orloff et al, December 2004).

DARPA/IXO Terrain Characterization was a two-year Congressional Plus-Up program that supported mobility, navigation and communications efforts of DARPA/Army Future Combat Systems (FCS) program. Their main objective in supporting the YOGI experiment was to provide FCS information about factors affecting vehicle operation in open areas as well as under foliage. Some of the terrain characteristics that could come into play are tree spacing and trunk diameter, surface roughness and moisture content, canopy height and density, roads, rivers, wires or towers. They will use the information to develop algorithms and techniques for determining and subsequently describing terrain characteristics relevant to vehicle operation. They plan to exploit and fuse the data from the multiple sensors to assist in terrain characterization (Orloff et al, March 2004).

HyPerspectives, Inc. is located in Bozeman, Montana and is a company specializing in exploiting natural resource applications and national security issues through the use of remote sensing technologies. The Yellowstone Ecological Research Center (YERC) was founded in 1998 and is a non-profit sister organization to HyPerspectives. They use remote sensing and other digital data sources to perform land studies that assist HyPerspectives in their own work. HyPerspectives assisted the YOGI data collection effort by providing ground truth and logistics support, performing terrain analysis on data collected for NRL, arranging for HyMap

hyperspectral sensor to collect data over the test sites, arranging for NASA/JPL AIRSAR to fly over test areas, and briefing U.S. Forest Services and obtaining special use permits for the related activities (Orloff et al, March 2004).

The Rapid Terrain Visualization (RTV) program is managed by the Joint Precision Strike Demonstration (JPSD) office. The RTV program supports rapid collection and exploitation of digital terrain data. As part of the YOGI experiment, RTV collected Light Detection and Ranging (LIDAR) and interferometric Synthetic Aperture Radar (IFSAR) data. Using these data, they were able to produce digital terrain maps, SAR backscatter imagery, and LIDAR intensity (Orloff et al, March 2004).

Calibration of the sensors was accomplished through various man-made objects such as aluminum corner reflectors, fabric panels, and tarps. Other objects imaged included cars, trucks, SUVs and other vehicles. Some were camouflaged, others were not, and they were in various locations that included out in the open or under foliage. The corner reflectors as well as some surrounding terrain were chosen as targets to simulate in DIRSIG and Xpatch.

3.1.1 Sensors

As mentioned earlier, the YOGI experiment was a multisensor data collection effort. NRL flew three optical systems on a P-3 aircraft: the WAR HORSE VNIR hyperspectral imaging sensor, the IRON HORSE SWIR hyperspectral imaging sensor, and the CA-270 EO-IR dual band reconnaissance camera. An Army RC-12 flew a VHF/UHF SAR system. RTV used a King Air to fly their LIDAR optical sensor and a DH-7 to fly their IFSAR sensor. NASA/JPL used a DC-8 to fly a SAR system and a twin engine Cessna was used with the HyMap optical sensors.

The work done for this paper modeled the NRL WAR HORSE and the RTV IFSAR sensors, therefore only those will be discussed in more detail. NRL's WAR HORSE (Wide Area Reconnaissance Hyperspectral Overhead Real-Time Surveillance Experiment) is a VNIR (visible near infrared) hyperspectral instrument. It is a pushbroom sensor that has a 1024x1024 Silicon Mountain Designs CCD camera and an American Holographic grating spectrometer. It operates at 40-60 Hz, with 1024 cross-track spatial pixels and 64 wavelength bands (Orloff et al, March 2004). The reader should refer to Table 3.1-1 for more detailed sensor specifications.

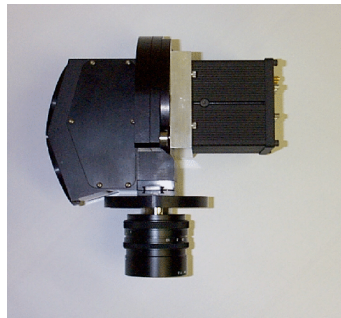


Figure 3.1-1 – NRL WAR HORSE (Courtesy of Space Computer, 2004)

CCD Camera	1024 x 1024 silicon CCD
Front-End Optics	75 mm lens
Field-of-view	9.3 degrees
Cross-Track IFOV	0.16 mrad
Spectral Range	500 – 950 nm
Spectral Bandwidth	11.4 nm (binned 8x1)
Spatial Pixels	1024
Spectral Channels	64
Frame Rate	40 frames/second
Scan Rate	0.025 seconds
Detector Element Size	0.012 mm
GSD at 6000 ft AGL	1.86 ft (0.566 m)
Swath width at 6000 ft AGL	1900 ft (579.12 m)

Table 3.1-1 – WAR HORSE specifications (Space Computer, 2004 and Orloff et al, March 2004)

The IFSAR (Interferometric SAR) sensor was developed by Sandia National Laboratories. It is capable of imaging in four bands: Ka, Ku, X and VHF/UHF. During the YOGI collect, it operated in the Ku band at 16.7 GHz.

The IFSAR sensor is capable of operating at a wide range of resolutions, depression angles, ranges and squint angles. VV and HH polarizations are both available when operating in the Ku band. Overlapped subaperture image-formation and phase gradient autofocus algorithms allow the IFSAR to form images in real time (Walker et al). Table 3.1-2 indicates the specifications of the sensor for the YOGI collect.

Capabilities	All weather, day/night operations
Swath width	1300 m
Frequency	16.7 Ghz (2 cm wavelength) Ku band
DEM GSD	3 m
Backscatter	0.75 m
Absolute vertical accuracy	1.4 m

Table 3.1-2 – NRL IFSAR specifications (Orloff et al, March 2004)

3.2 Common Scene Development

One of the objectives of this research was to determine if a common geometry could be created that could be modeled in both an EO and a SAR simulation tool. In order to determine the feasibility of this, a common scene first had to be created in a computer aided design (CAD) modeling tool. The tool used in this research is called Rhinoceros, or Rhino for short. It was decided that a single object on a ground plane should be tested for compatibility in the two simulation tools as a starting point. The single object chosen was the 16-foot corner reflector that was imaged in the YOGI dataset, shown in Figure 3.2-1. The Rhino CAD format was easily converted to the object format that DIRSIG recognizes for the EO simulation. Once it was determined that more steps were required to get the Rhino format into an Xpatch-recognizable format, a converter tool was written that converted the DIRSIG object format into the Xpatch facet format. The corner reflector was converted into each of these formats and run in their respective tools, indicating that it is possible to run a common geometry in both tools. Knowing this, a more complex scene was developed to incorporate other objects and backgrounds, shown

in Figure 3.2-2. However, more issues were encountered in the SAR simulations for the complex scene, which are detailed in the next chapter.

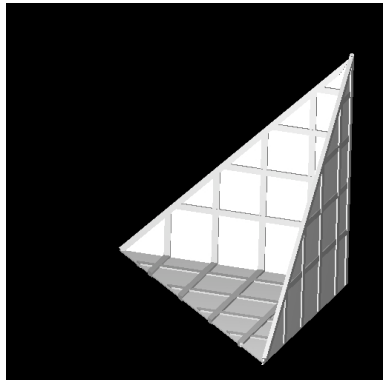


Figure 3.2-1 – Model of corner reflector

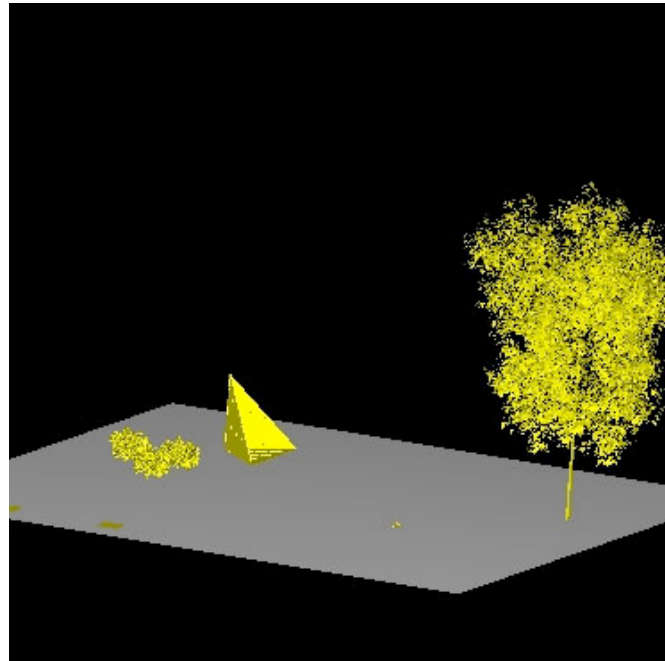


Figure 3.2-2 – Scene used for simulations

3.3 Basic Scene Development for DIRSIG

Part of the data collection in YOGI occurred at a place called Fisher Creek, an area that is located about midway between the bottom of a valley and Sheep Mountain. This area consisted of various types of land cover, including dirt and gravel roads and trails, densely forested areas, open grassy areas, regenerating areas from fires, and downed wood. Various objects, or targets, were imaged throughout this area as part of the data collection. The first scene constructed for research that is the focus of this paper consisted of a 16-foot trihedral corner reflector, to model the actual corner reflector in the YOGI dataset in an open area of Fisher Creek. The corner reflector was constructed in Rhino. In addition to the corner reflector, a flat plate was also constructed in Rhino, upon which the corner reflector would sit. Using a program called Bulldozer, which is part of DIRSIG, the corner reflector was attributed with the material

type of aluminum. It was placed flat on the middle of the plate, which was also attributed with various materials through Bulldozer. The model of the 16' corner reflector can be seen in Figure 3.3-1. An image of the actual corner reflector used in the YOGI dataset can be seen in Figure 3.2-2, however the reflector modeled was one from an open field location. Figure 3.3-4 shows the 15" CAD corner reflector and Figure 3.2-4 shows the YOGI dataset 15" reflector.

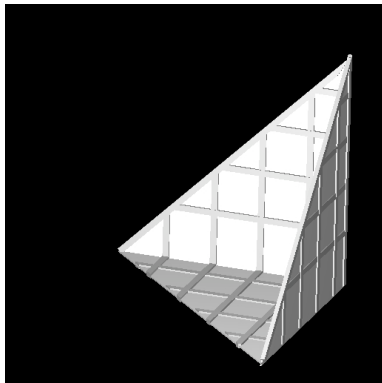


Figure 3.3-1 – Model of 16-foot corner reflector



Figure 3.3-2 – Actual 16-foot corner reflector

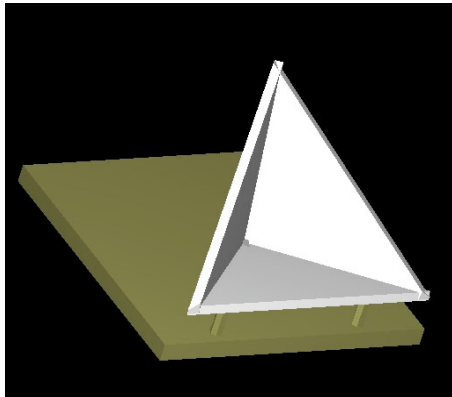


Figure 3.3-4 – Model of 15" corner reflector



Figure 3.3-4 – Actual 15" corner reflector

The scenes constructed all included some type of corner reflector. The first scene was the 16' aluminum corner reflector on grass. The second, more complex scene consisted of the 16'

corner reflector, a 15" corner reflector on a wood stand, two types of trees, and two calibration panels. The calibration panels were inserted to help alleviate display issues in ENVI, which tries to stretch the RGB display colors to a minimum and maximum that it arbitrarily chooses. By adding a dark and light calibration panel in the scene, it has a minimum and maximum already built in so ENVI doesn't have to choose them arbitrarily. This scene was discussed briefly and displayed in the previous section, shown in Figure 3.2-2.

With the simple scene constructed as a DIRSIG-compatible object database file (.odb), a configuration file (.cfg) was constructed to run with DIRSIG. It was configured to simulate July 28, 2003 at a ground elevation of 2.634 km above sea level and coordinates of latitude +45.041N and longitude -109.913E, all of which was meant to model the YOGI dataset at Fisher Creek (Orloff et al, March 2004). One thing to note about DIRSIG is that for the longitudinal coordinates, west is positive. Therefore, even though the scene at Fisher Creek occurs at a positive latitude and negative longitude, to model it correctly in DIRSIG, the longitude should be input as a positive number.

The environment was set to model a mid-latitude summer with 23 km visibility and no clouds or rain. Another iteration of the environment included changing the MODTRAN run to simulate mid-latitude winter with 100 km visibility to simulate the dry air of Fisher Creek. The actual data was taken on a day of no rain and minimal to no clouds. The platform was set up to simulate the actual NRL WARHORSE sensor, with a focal length of 75 mm and a scan rate of 0.025 scans per second. The sensor was simulated to be flying east at an altitude of 4419.60 m and speed of 22.67120 m/s. The speed was determined by taking the ground sample distance (GSD) of WARHORSE, which is 1.86 feet or 0.567 meters, and dividing it by the scan rate of the instrument, 0.025 scans per second. This would result in ideal sampling of the ground, with the sensor moving along at a rate that would result in no overlapping or missed data. A flow chart illustrating the DIRSIG configuration file development is shown in Figure 3.3-5.

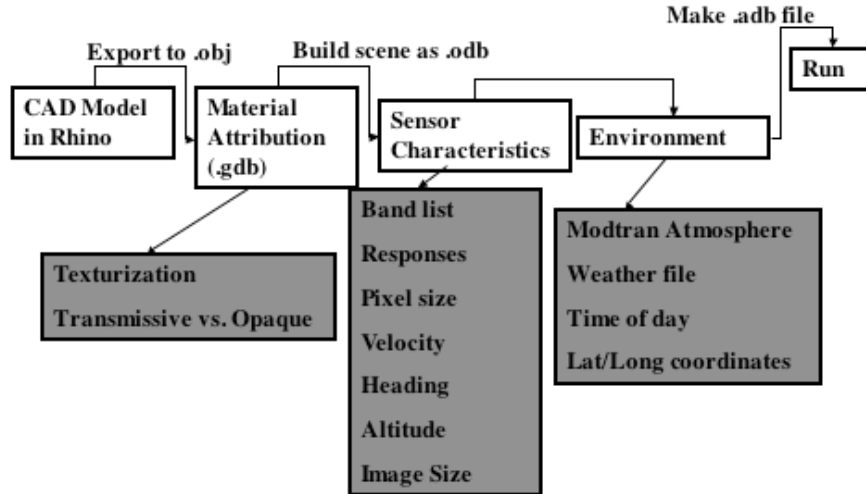


Figure 3.3-5 – Flow chart of DIRSIG configuration file

3.4 Basic Scene Development for Xpatch

DIRSIG uses the CAD model in a .obj format that is turned into a .gdb format through the use of Bulldozer. The .obj format is an export type available in Rhino that was compatible with DIRSIG. Xpatch uses a .facet or .iges format as its input CAD model. Rhino does not export in a format that was compatible with Xpatch, therefore a tool was created for Bulldozer that could convert a .obj format to a .facet format compatible with Xpatch. It was important during the conversion step not to create additional facets, i.e. one facet is made into two smaller facets, because a greater number of facets in a scene resulted in increased run times in Xpatch. This conversion step answered one of the questions of the research about whether a common geometry could be used in both tools. It is possible to get a common geometry running in both tools with this converter, since once the model is exported to the DIRSIG format, it can easily be converted from that to the Xpatch format, thereby making it recognizable in both tools.

Once the CAD model was converted to the Xpatch format, it was attributed with appropriate material parameters within the Xpatch GUI. The material parameters are described by permittivity and permeability values for the operating wavelength of 16.7 GHz for this

research. The next step is to describe the electromagnetic physics of the simulation, to include how many rays per wavelength should be traced towards the object and how the first bounce integration is handled. The user also specifies in this section the maximum number of bounces Xpatch should calculate, in case there is an object in which there could be hundreds of bounces, due to a feature such as an aircraft inlet that would cause run times to multiply. The user also specifies which bounces should contribute to the final scattered field. To cut down on run times, the user can specify just the first and last bounces for contributions, however this inherently decreases the accuracy of the returns. Within the EM physics section, there is also the option to handle edge diffraction for objects, however in the current version of Xpatch, the edge diffraction is only accurate for PEC (perfect electric conductor) materials.

Next in setting up the Xpatch run is to specify the output type and domain. The domain can either be handled in frequency or time and the output types are RCS, SAR Image, Range Profile, and Scattering Centers. This research utilized SAR Image outputs in the frequency domain. The operating frequency as well as bandwidth, resolution, and pixel size are also specified in this group of settings. The operating frequency modeled was 16.7 GHz with 0.75 m resolution for square pixels.

The final step before running the SAR simulation is to set up the aspects, or look angles, of the SAR system. All simulations were run as mono-static (one antenna for transmitting and receiving) with the system looking directly into the inside corner of the reflector from 45 degrees elevation. A flow chart illustrating the Xpatch input file process is shown in Figure 3.4-1.

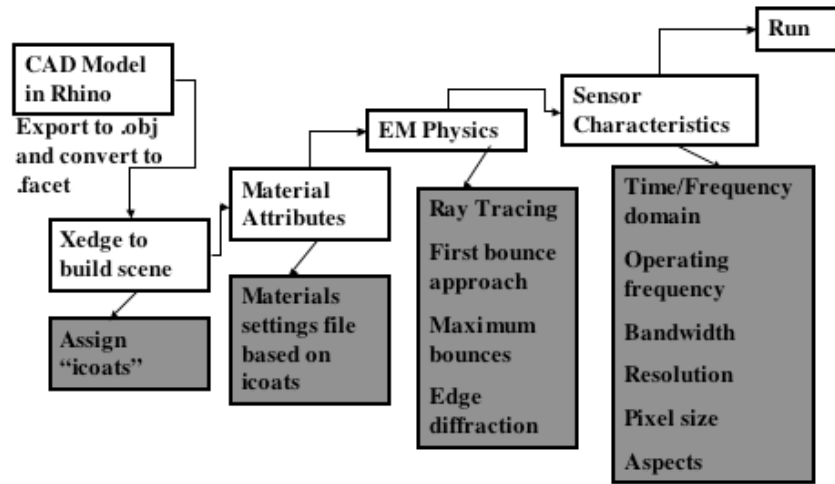


Figure 3.4-1 – Flow chart of Xpatch input file

4 Results

This section will describe, in detail, the results obtained using the approach laid out in the previous chapter. It will begin with a discussion on the details and results of the EO simulations for a simple scene. Following that will be a parallel discussion on the SAR simulation results for an object within the scene used for the EO simulations. The issues encountered in modeling the entire scene in the SAR simulations that was used in the EO simulations will be discussed in this section as well as in more detail in the next chapter.

4.1 Electro-Optical Scene Comparisons

The WARHORSE data included a vast amount of area and targets, and therefore, as mentioned in the previous section, it seemed appropriate to select only a few items of interest to model in DIRSIG and compare to the real data. Since one of the objectives of this research effort was to determine the feasibility of taking a common geometry and modeling it in an EO simulation tool as well as a SAR simulation tool, it seemed most useful to keep the scene as simple as possible, so the issues that panned out were a result of the limitations of the tools, not a result of the complexity of the scene. Therefore, the large 16-foot corner reflector, the smaller 15-inch reflector, and a few types of trees were placed on a ground plane and modeled appropriately. In addition to these targets, two calibration panels, one dark and one light, were added to the corner of the ground plane to assist in proper display in ENVI. A variety of DIRSIG simulations were run, varying the material properties of the grass and corner reflectors, as well as modifying aspects of the atmosphere to best match the real data.

4.1.1 DIRSIG Response Files

DIRSIG uses detector spectral response files when the user wishes to specify a response other than an ideal one. The response file also allows the user to specify different responses for each wavelength if desired. For the response file created to mimic the WARHORSE sensor, the minimum wavelength was 0.434 microns and the maximum wavelength 1.155 microns, with a channel width of 0.01144 microns and Gaussian shape. The spectral response for each band was

set to 0.01144 microns, which was the response of WARHORSE found in the literature (Stellman et al, 2001). Also, the shape of each channel was set to a Gaussian shape, since DIRSIG allows for either that or a triangular shape in the response file.

The real data shown in the figures represents the radiometrically-calibrated WARHORSE data accomplished by the Naval Research Laboratory (NRL). This was accomplished by calculating a gain and offset for each pixel on the focal plane of the sensor. Using this gain and offset as well as the spectral radiance of an integrating sphere, the raw data were converted to the spectral radiance of the sensor (Orloff et al, October 2004). The units of the WARHORSE data are micro Watts/(cm² sr μ m). Also in the response file used in DIRSIG is the option to change the gain of the sensor. The gain was set to 10⁶ to convert the default DIRSIG units of W/(cm² sr μ m) to micro W/(cm² sr μ m) so radiance values in both the WARHORSE data and the simulated data would be in the same units.

4.1.2 Texturization

DIRSIG offers many options for making simulated data behave more like real data. One of these options is texture mapping. This mapping allows the user to give a certain material spatial variation using reflectance curves associated with that material. The inhomogeneous nature of most materials gives rise to spatial variations in reflectance. This property, as well as changes in orientation, surface structure, and shading all result in the texturized appearance of some materials. DIRSIG utilizes a database of reflectance curves for a given material as well as a bi-directional reflectance model to simulate texture in the resulting imagery (DIRSIG User's Manual, 2004). The methodology of texturization is illustrated in Figure 4.1-1.

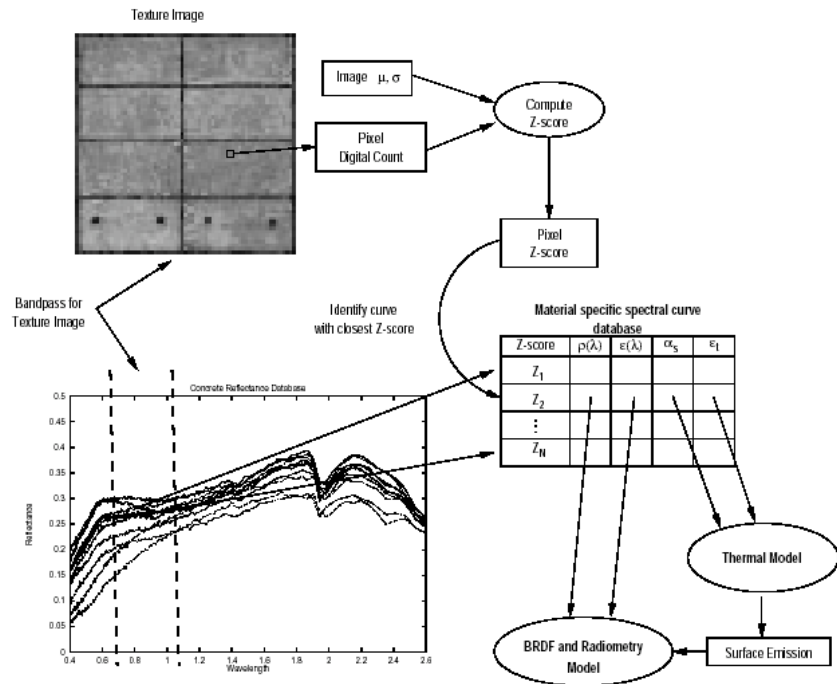


Figure 4.1-1 – Flow diagram of texture application in DIRSIG (DIRSIG User’s Manual, 2004)

In this research, a texture map was used to show the variation in the grass background. During the YOGI collect, a field spectro-radiometer was used to take spectral reflectance measurements of various terrain and other objects in the areas imaged. The device used was an Analytical Spectral Devices (ASD) FieldSpec Pro FR instrument. The ASD was used to take reflectance data of various objects in the scene, including vegetation. These reflectance curves were used to generate the database used by DIRSIG for the texture map.

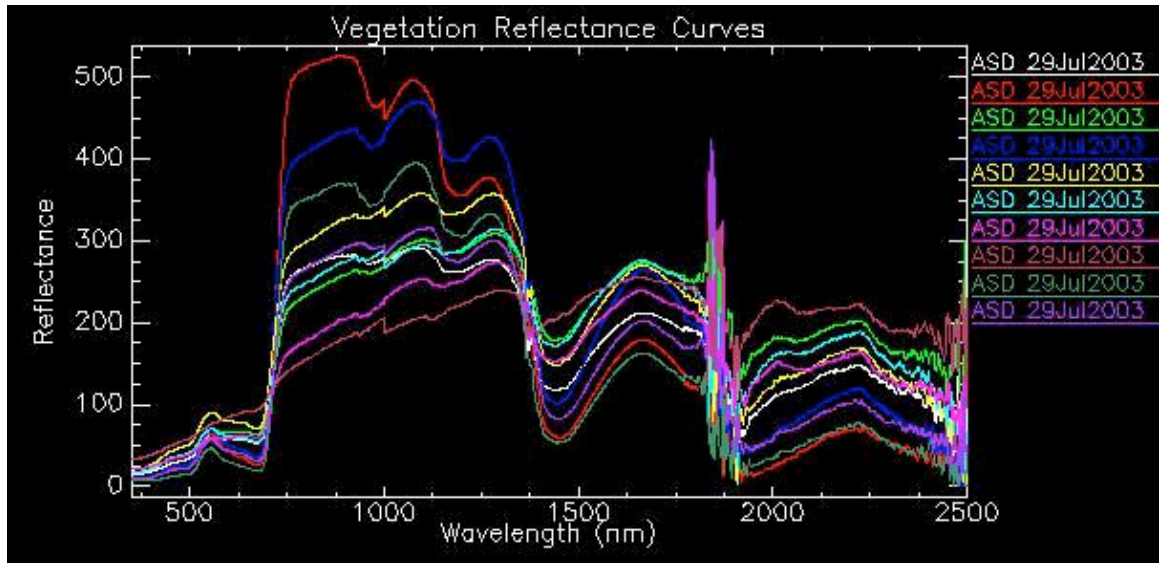


Figure 4.1-2 – Vegetation reflectance curves used for DIRSIG texture map

Since the exact location of each of these ASD measurements for the vegetation was not annotated in the documents accompanying the ground truth, some experimentation had to be done with the various reflectance curves to determine which combination resulted in the most realistic looking vegetation. It was mainly an iterative process that involved initially using all the vegetation curves, running the simulation, determining if the resulting radiances were too high or too low, and removing curves as necessary. Using all 10 reflectance curves shown in Figure 4.1-2 resulted in vegetation with radiance values much higher than in the WARHORSE data. Therefore, it was determined that removing some of the higher reflectance curves within the emissivity file for the vegetation might result in more closely matched radiance values. After several iterations that involved removing one curve at a time, it was determined that the best agreement between simulated and real vegetation occurred with only 7 of the 10 curves shown. The seven chosen were the seven lowest reflectance curves. The need for eliminating some of the ground truth curves arose because these curves were actually taken from a different part of the data collection area than Fisher Creek, and were not necessarily representative of the vegetation around the corner reflector.

4.1.3 Transmissive Materials

The large 16-foot corner reflector modeled in the WARHORSE data was actually a mesh material, whereas the CAD file of the simulated 16-foot corner reflector was solid aluminum. DIRSIG allows the user to attribute an object with a material map that has null values, which would be useful in modeling holes in mesh. While DIRSIG 4.0 allows the user to do so on a vertical surface as well as a horizontal surface, DIRSIG 3.6, which was the version used for this research, can only do so on horizontal surfaces. Since the corner reflector has two vertical faces and one horizontal face, the material map with null values could not be used to model the mesh material. Though the horizontal surface is the main surface the detector is imaging, the effects of the skylight passing through the mesh in the vertical surfaces and the effect this had on the resulting shadow, also needed to be taken into account. Therefore, another way to try to achieve the same effects of holes is to make the solid material optically transmissive rather than geometrically transmissive, allowing some of the light to pass through the material. This was the approach used to model the mesh material in this research.

The details of the exact measurements of the corner reflector, other than the overall height of 16 feet, were not available as part of the ground truth. Therefore, some estimates had to be made from the ground photographs of the reflector. One of these estimates was the thickness of the walls. These were estimated to be approximately one-quarter inch thick. The percent transmission of the aluminum was set at 75%, which seemed reasonable since there were more holes than solid material, thereby allowing quite a bit of light to pass through the openings. Other percentages of transmission were also modeled, such as 50% and 99% to see which resulted in the best spectrum for the aluminum, and 75% seemed to model the aluminum most accurately.

DIRSIG utilizes an extinction file to model transmissive materials. To convert transmission values to extinction coefficients, the following equation was used:

$$\beta = \frac{-\ln(\tau)}{d} \quad (4.1-1)$$

where

β extinction coefficient

d thickness of the material in kilometers

τ percent transmission

4.1.4 Aircraft Motion Smear

As mentioned in the previous chapter, the aircraft was originally modeled to be flying at ideal speed, 22.67 m/s. In addition to the images resulting from this platform speed, a faster, more realistic speed was modeled as well. The reason for this was twofold; the P-3 aircraft on which the WARHORSE sensor flew could not reasonably fly at 22.67 m/s, and the actual WARHORSE images exhibit smear in the direction of aircraft motion due to a faster velocity than 22.67 m/s. Therefore, it seemed reasonable to model the simulated data at both the ideal velocity and the actual velocity.

The actual velocity of the P-3 during data collection was not known; therefore a reasonable estimate was made by observing the length of smear of the data in the direction of aircraft motion. The pixels appeared to be about four times as long as they were wide, so the velocity was chosen to be four times ideal velocity, or 90.71 m/s. The DIRSIG configuration file was set up to move the platform at that velocity, and the result was a compressed image, since only one quarter of the data was collected as compared to flying at ideal speed. As a comparison, the platform was simulated to be flying at three and five times the ideal speed, to determine if four times really was the best estimate. Indeed, three times the ideal velocity resulted in pixels that were not elongated enough as compared to the WARHORSE image, and five times resulted in pixels that were too long.

In the georectified WARHORSE image, which was the image used for comparison to the simulated data, it appeared that in correcting for missed data due to aircraft motion, an interpolation was performed to fill in the missing data. The actual interpolation was not listed in the literature accompanying the data collection, but there was little to no spectral variation among the four interpolated pixels in the along track direction of the sensor. Therefore, it was decided that replicating each line of data four times to fill in the missing data in the simulated image would result in similar data. To simulate this from the compressed DIRSIG image, the data were exported to IDL. A new array was created that was four times as large as the compressed image in the direction of motion. This new array was populated with the data from the compressed image, where each line was duplicated four times, which resulted in an image with stretched

pixels to match the WARHORSE data. An example of the IDL code and comments is shown below, assuming the compressed image was already exported to IDL and named “compressed” and the new array is named “new”. Lines beginning with “##” are comments:

```

>print,size(compressed)
      3           80           20           64
      ## number of dimensions, x number of pixels, y number of pixels (aircraft
      ## motion direction), z number of bands
>new=fltarr(80,80,64)
      ## creates an array with floating point numbers with x and z dimensions the same
      ## as the compressed image and y dimension four times that of the compressed
      ## image
>for i=0,19 do new[*,4*i,*]=compressed[*,i,*]
>for i=0,19 do new[*,4*i+1,*]=compressed[*,i,*]
>for i=0,19 do new[*,4*i+2,*]=compressed[*,i,*]
>for i=0,19 do new[*,4*i+3,*]=compressed[*,i,*]
      ## populates “new” array with data from “compressed” array, duplicating each
      ## line four times

```

The “new” array was then imported back into ENVI for viewing and saving purposes.

4.1.5 Point Spread Functions

In order to model the spectral and spatial interactions of neighboring pixels, a point spread function (PSF) was incorporated into the DIRSIG configuration file. The PSF is the response to a point source. In other words, it is the system’s ability to model a point source of light. In the ideal case, the system would produce a point of radiance; however in actual systems, the point source is imaged as a blur spot. The amount of “spread” of the point source into the blur spot is described by its point spread function (Schott, 1997).

Each pixel in the simulated imagery was oversampled twice (2x2) and the PSF was considered to be well behaved, meaning it did not vary with wavelength. The actual WARHORSE PSF was unknown, and therefore different PSFs were experimented with to determine the best match with the WARHORSE data. Oversampling of three, four and five times were attempted, however the 2x2 seemed to produce the best agreement with the real data. This is most likely because the actual WARHORSE data were undersampled due to the velocity of the

aircraft. Therefore, although more oversampling should result in more accurate comparisons, since the simulated data are being compared to undersampled real data, the two-times oversampling resulted in the best agreement.

4.1.6 Spectral Comparisons

Various iterations of DIRSIG configuration files were created, varying material properties and sensor characteristics to try to model the WARHORSE data as closely as possible. Figure 4.1-3 depicts a simulated electro-optical scene from DIRSIG of the targets and background chosen for the scene. The trees were chosen from DIRSIG Microscene and Megascene tiles in order to compare the ability of the simulated sensor to model vegetation other than grass. The Microscene Arrowwood trees were too small to be modeled reasonably with the WARHORSE-like sensor, and therefore the larger Silver Maple was added to the scene. Figures 4.1-4 and 4.1-5 show the effects of smear on the DIRSIG image as compared to the WARHORSE image, resulting from a velocity four times that of the ideal velocity. Figures 4.1-6 through 4.1-8 show spectral comparisons between the simulated DIRSIG data and the WARHORSE data. The comparison was done on a 10 x 10 averaged region of pixels that surrounded a chosen pixel in both the simulated and real scenes. The root mean squared error (RMSE) is shown for each as well, which is normalized to the mean of the WARHORSE data.

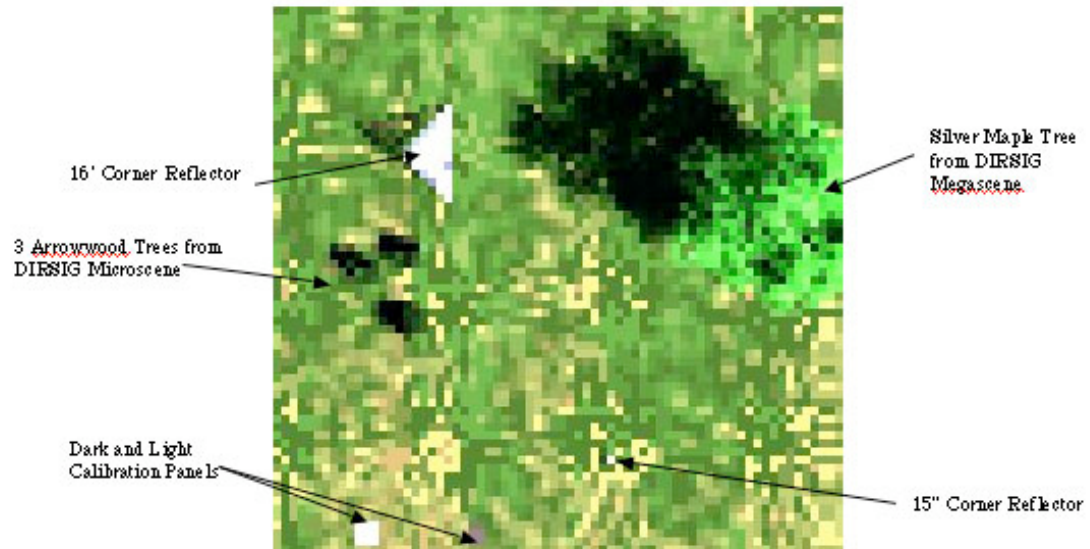


Figure 4.1-3 - Rendered electro-optical scene from DIRSIG with ideal aircraft velocity

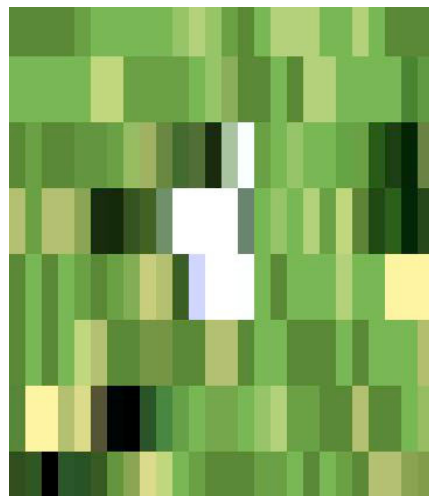
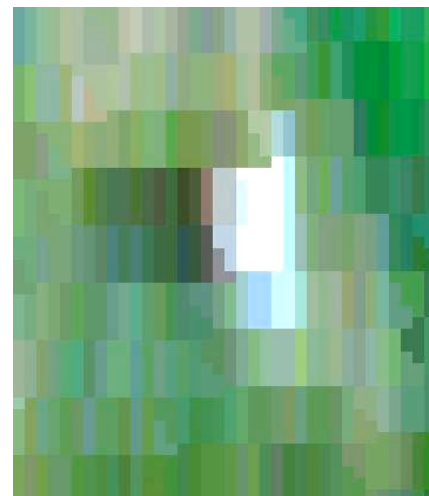


Figure 4.1-4 – DIRSIG corner reflector with



smear due to aircraft motion

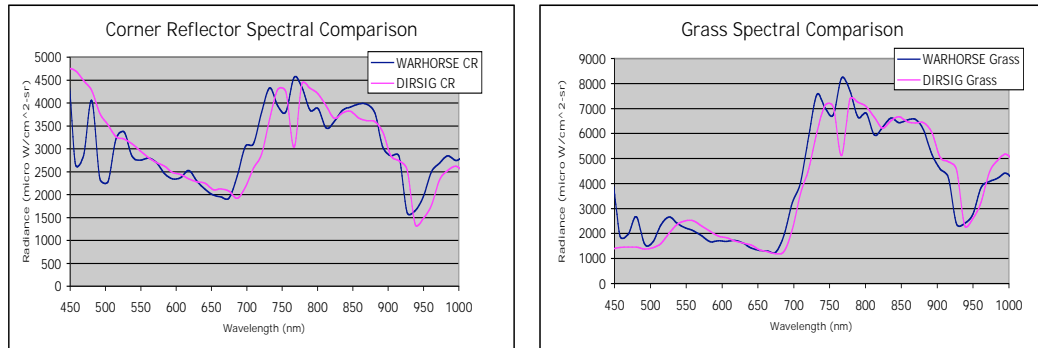


Figure 4.1-6 – Corner Reflector Spectral Comparison (RMSE = 3.01%)

Figure 4.1-7 – Grass Spectral Comparison (RMSE = 2.85%)

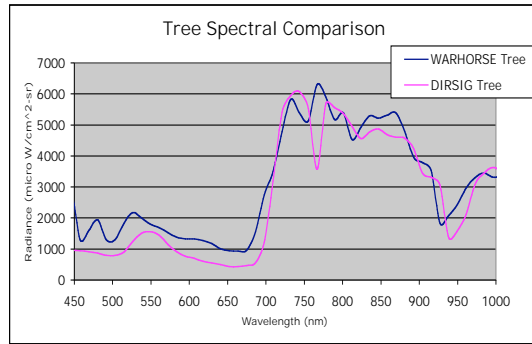


Figure 4.1-8 – Tree Spectral Comparison (RMSE = 3.41%)

The results shown in the Figures 4.1-6 through 4.1-8 were attained by using transmissive aluminum and texturization of the vegetation. It should be noted that the simulated data exhibits a deeper trough at 760 nm than the WARHORSE data. Both water and oxygen absorption features occur at 760 nm, though the water absorption feature also occurs at 940 nm. Since the 940 nm features in both the simulated and actual data seem to be in agreement, it would indicate that the oxygen absorption is the cause of the discrepancy at 760 nm. This could signify that there is too much oxygen in the simulated atmosphere, either because the sensor is too high above the ground or the ground elevation is not high enough. Both these altitudes were varied, to the point where the sensor was flying only 15 feet off the ground, and the trough was still too deep. This indicates that perhaps the DIRSIG data are correct and that its possible the WARHORSE data are

exhibiting anomalous behavior. For example, the peak in the WARHORSE data immediately following the trough at 760 nm seems slightly high, which could be “pulling” up the trough at 760 nm, causing it to appear shallower than it should be.

Another hypothesis involving the 760 nm trough discrepancy was that the 8-times spectral binning of the actual WARHORSE sensor caused the spectral response shape to look more rectangular than Gaussian, and perhaps changing this would smooth out the trough, causing it to be more shallow. The response file for the DIRSIG run was changed to model this rectangular shape; however, the resulting image exhibited no significant change in spectral shape, and the trough at 760 nm was just as deep as with the Gaussian-shaped response.

The reader should also take note that there is some offset between the real and simulated data, showing up most notably at peaks and valleys. This is most likely due to spectral calibration error from slightly different band centers in the WARHORSE data when the sensor was flown as compared to what is reported in the literature for the sensor’s parameters due to spectral calibration issues. Features at 940 nm, 760 nm, and 550 nm were chosen as comparison features to quantify the offset. A region at each of these wavelengths was chosen in the WARHORSE data, then oversampled and correlated with the DIRSIG data to determine the spectral calibration error. These steps were performed on the grass, tree and corner reflector spectra to determine if the offset was constant. The resulting offset was 11.5 nm, indicating that the WARHORSE data were off by one channel. The WARHORSE data were then shifted to the right by 11.5 nm, and the errors were recalculated, in the hopes that they would decrease since the offset was contributing to the error. The results are shown in Figures 4.1-9 through 4.1-11.

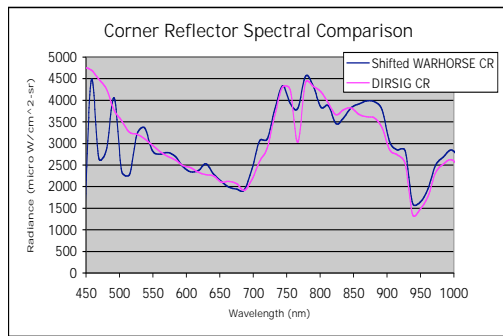


Figure 4.1-9 – CR spectral comparison for shifted data (RMSE = 2.19%)

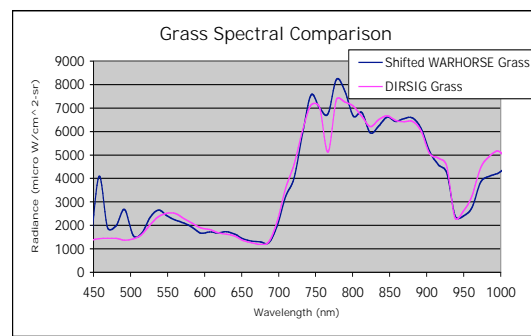


Figure 4.1-10 – Grass spectral comparison for shifted data (RMSE = 2.21%)

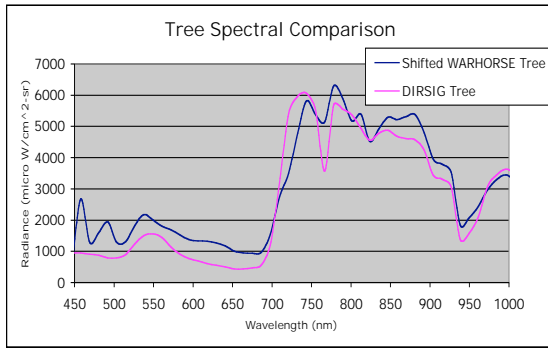


Figure 4.1-11 – Tree spectral comparison for shifted data (RMSE = 3.24%)

The results shown in Figures 4.1-9 through 4.1-11 exhibit a much better agreement than the unshifted data, with a lower percent error. The percent error improved up to 17%, in the case of the corner reflector, indicating that the spectral calibration error was in fact a significant contributor to the error. In all cases of spectral comparison, the WARHORSE data are exhibiting some peaks and troughs in the blue wavelength region (around 475 nm) that are not expected. This could be noise or some sensor artifact that was not reported, therefore the DIRSIG data do not exhibit these same peaks and troughs in that region.

Overall, the simulated DIRSIG data matches up very closely to the WARHORSE data. This demonstrates that it is possible to take a CAD model representing a real area and run it in an EO simulation tool, modeling the real sensor characteristics, and obtain imagery that reasonably matches the real data. These images, combined with simulated images from other types of sensors, could then serve as a cost effective way to experiment with fused imagery techniques.

4.2 Synthetic Aperture Radar Scene Comparisons

As part of the objectives of this research, it was to be shown that a common geometry could be rendered in both the EO simulation tool and the SAR simulation tool. The 16-foot corner reflector was successfully rendered in Xpatch using two different types of materials. However, the run times associated with these runs were excessively long, on the order of 35 hours. Increasing the complexity of the scene, even in the addition of a ground plane, increased

the run time so that it was averaging 1% per day. These runs were halted before completion since 100 days of run time seemed unreasonable.

4.2.1 CAD Conversion

All geometries used in Xpatch originated in Rhino and were the same geometries used in DIRSIG. Rhino has an export option that allows the user to export a Rhino CAD drawing into any number of other file types, depending on the desired use. While Rhino offers the ability to export to the DIRSIG compatible format of .obj, it does not offer the ability to easily convert to an Xpatch-friendly format, namely either .facet or .iges. Therefore, a conversion tool was established that converts a .obj format to a .facet format in Bulldozer, thereby easily taking any geometry that can be used in DIRSIG and making it usable in Xpatch (Brown, 2005).

4.2.2 Material Attribution

In some of the first runs in Xpatch of the 16-foot corner reflector, the default material type of PEC (perfect electric conductor) was used. This was in the hopes that aluminum could be modeled as a perfect electric conductor, but it was determined that this resulted in returns that were too high as compared to the IFSAR data. Therefore, it was decided that a material settings file would need to be used in Xpatch to attribute the corner reflector with material properties that were closer to some type of aluminum.

As the ground truth in the YOGI data did not include specifics on the type of aluminum that comprised the corner reflectors, a reasonable estimate had to be made as to the dielectric properties of the particular type of aluminum needed to model the reflector properly. The values chosen to model the aluminum, found in (Davis, 1993), were a permittivity of 9.5 and permeability of 1.0 for 16.7 GHz, which is the frequency at which the IFSAR data were taken, and therefore was the frequency chosen for the Xpatch simulations.

4.2.3 Platform Configuration

Xpatch was set to output a SAR image at 16.7 GHz with 255 frequency steps. The down range resolution was set at 0.75 m, which was the resolution reported for the IFSAR sensor. The cross range values were set the same as down range, resulting in square pixels. The radar was set to be mono-static, meaning one antenna was used for transmitting and receiving. Both the azimuth and elevation sweeps were configured for 45 degrees so that the sensor was pointed down into the inside corner of the reflector. The justification for choosing only one aspect angle to model the SAR image was that Xpatch was designed to use the center frequency specified by the user to extract the necessary aperture angle and individual angles for all the necessary frequency spectra. It does this by incorporating the parameters such as resolution, angular span, angular increment and other signature settings input by the user (Xpatch User’s Manual, 2004). No roll, pitch, or yaw of the platform was included since the IFSAR data had already been corrected for those.

4.2.4 IFSAR Calibration

The IFSAR pixel numeric value was actually an 8-bit calibrated value and therefore could not be compared directly to the Xpatch dBsm (decibels square meter) output. In order to convert the IFSAR 8-bit values to dBsm, each value had to be squared to get the original magnitude of the 16-bit image. This value was then multiplied by the Sandia Laboratories reported calibration parameter of 0.000387 for the data to convert the 16-bit value to meters. To convert this into dBsm, $20 \times \log_{10}(0.000387 \times n^2)$ was applied, where ‘x’ is the value in meters obtained from the previous step. These steps resulted in pixel values in dBsm that could be directly compared to the Xpatch outputs. For clarity, this equation is laid out below (Equation 4.2-1), where “n” is the pixel value in the 8-bit calibrated IFSAR image.

$$\text{Value(dBsm)} = 20 \times \log_{10}(0.000387 \times n^2) \quad (4.2-1)$$

4.2.5 SAR Profile Comparisons

After the calibration steps were completed on the IFSAR data to convert to dBsm, slices of both that and the Xpatch data were compared. Figure 4.2-1 shows the same area of Fisher

Creek from both the WARTHORSE and IFSAR sensors. Figure 4.2-2 shows the same IFSAR image with the corner reflector in the zoomed box for clarity. Also in this figure is the SAR image resulting from the Xpatch simulation. Vertical slices were chosen from both the IFSAR and the Xpatch rectangles that represent the corner reflector since the simulated corner reflector was oriented to match the real reflector. The slices were chosen to model the center lobe of the return only, and excludes any of the ringing shown in the Xpatch simulated data. The reason for choosing slices was to compare the profiles of the data, which should be in a Sinc-like shape in keeping with SAR theory. Various slices were compared for a number of the 16-foot corner reflectors in the YOGI data to determine if the Xpatch data closely matched any of them, since changes in clutter and orientation would affect the resulting backscatter. These comparisons are depicted in Figure 4.2-3.

The Xpatch aluminum slice as well as the data labeled ‘Xpatch 2’ and ‘Xpatch 3’ are for three separate slices of the same SAR output of the Xpatch run depicting the corner reflector in free space. The data labeled as Xpatch with clutter is for that same corner reflector sitting on an Xpatch-generated ground plane to try to simulate the ground clutter that the actual corner reflectors experienced in the IFSAR data. These data exhibit a noticeably smaller magnitude than the IFSAR data or the Xpatch data for the corner reflector in free space. Though it seems more logical that the reflector on a ground plane with clutter would more closely match the real data, the results indicate otherwise. This could be because the dielectric properties chosen to model the aluminum are not close enough to the actual aluminum and therefore when the reflector is modeled closer to the actual reflector as far as ground clutter, the data are not matching up the way they should. The other possibility for the discrepancy is that Xpatch is not the best simulation tool for modeling scenes as opposed to just objects. This is because, as mentioned in the background section, Xpatch models well electrically large objects (on the order of 10λ or more) but is less accurate at modeling electrically small objects, such as the grass chosen for the ground clutter.

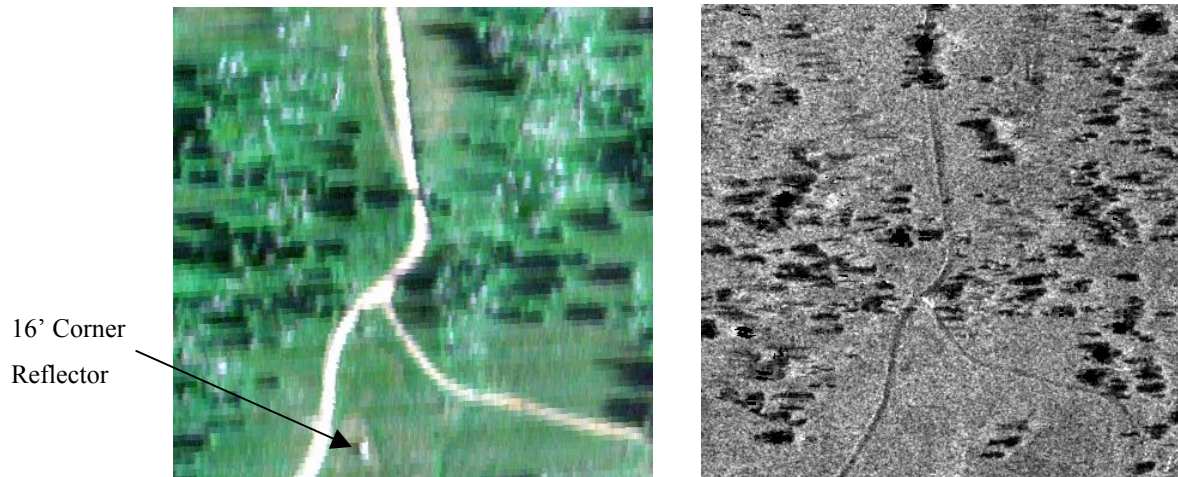


Figure 4.2-1 – WARHORSE (left) and IFSAR (right) images of Fisher Creek

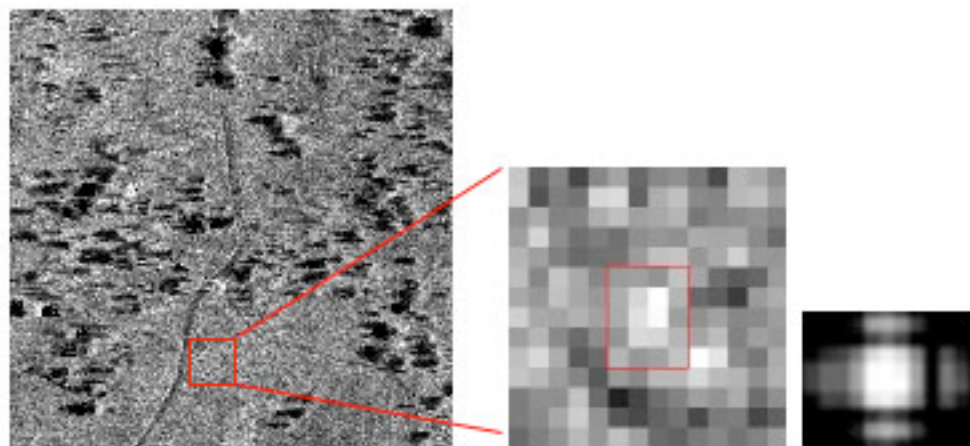


Figure 4.2-2 - IFSAR with corner reflector in zoomed box (left and middle) and Xpatch SAR for 16' corner reflector in free space

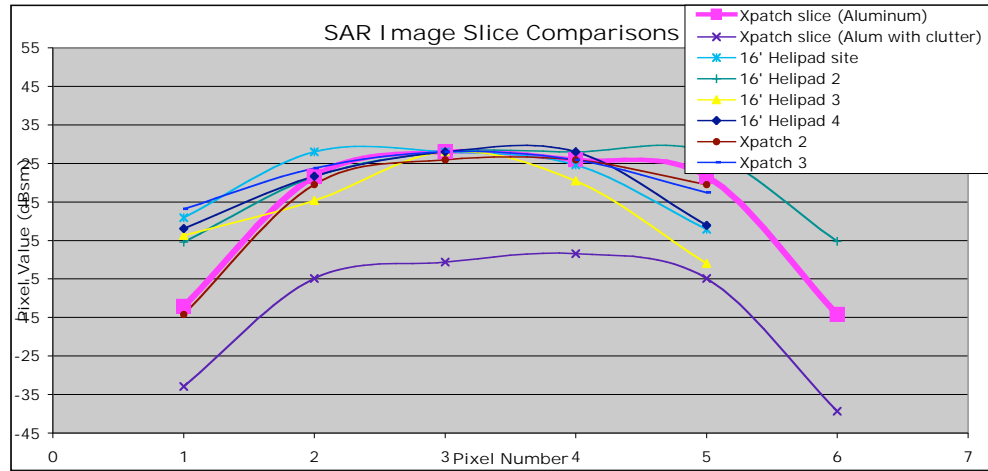


Figure 4.2-3 – Xpatch and IFSAR data comparisons

The multiple comparisons shown in Figure 4.2-3 make it difficult to see the best comparison out of all of the slices and reflector locations, therefore the closest match was chosen to be shown separately as compared to the IFSAR data. This is portrayed in Figure 4.2-4.

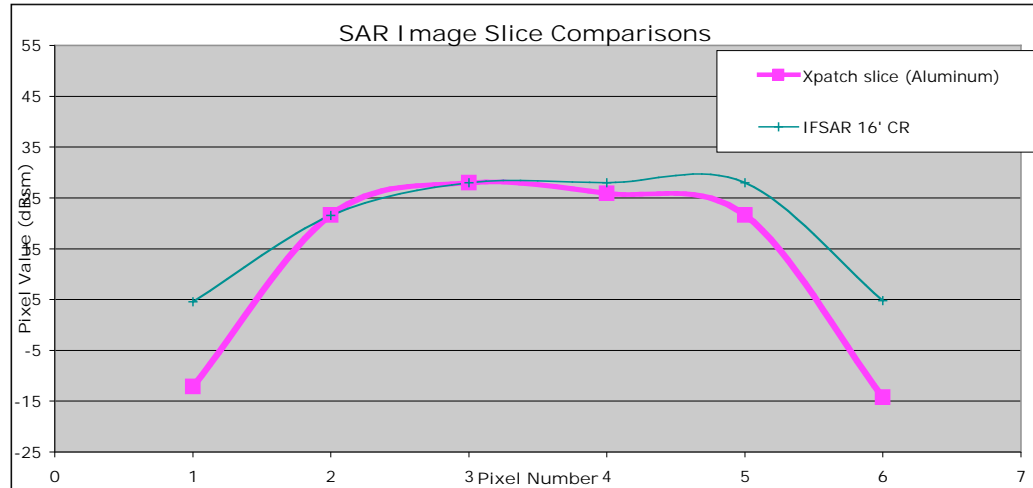


Figure 4.2-4 – Single slice Xpatch and IFSAR comparison (RMSE = 2.28%)

Though the magnitudes of the IFSAR and Xpatch slices are similar and the RMSE is only 2.28%, there is some discrepancy in the pixels depicted to the right of the middle as well as the

left edge of the slice. There are several possible reasons for this. Phase error associated with the IFSAR sensor could be affecting the sidelobes of the return, whereas the Xpatch runs were accomplished with no phase error. The IFSAR data makes it difficult to examine the sidelobes because the resolution and clutter of the image make it difficult to determine where the sidelobes end and the clutter begins. Without a clear picture of the sidelobes, it is not discernable whether phase error exists in the image or not. This phase error could have occurred during motion compensation, post processing of the data, inherent system errors, or processor effects. Even if these factors were quantified in the accompanying YOGI collect data, Xpatch does not have the ability to account for sensor effects or motion (Xpatch Training Course, 2004).

Another possible reason for the discrepancies between the simulated SAR data and the IFSAR data, namely the broadening of the data that is not present in the Xpatch simulations, is the weighting that was applied to the real data. Different types of windowing will cause different broadening of the center lobe of the return, as well as affect the amplitude of the sidelobes, which is the main purpose of windowing. Xpatch has the ability to model windowing, but only in the time domain, not the frequency domain, which is the domain used for the simulations in this research. Therefore, it was not possible to experiment with different windowing parameters to try to more closely match the IFSAR data.

4.2-5 ~~Figure~~ the effects of different types of windowing on the sidelobes and main lobe of a function. The δ and θ symbols represent the resolution and squint angle, respectively. The example shown is for a normalized resolution of 1.0 and a broadside squint angle (i.e. perpendicular to the flight line). Both types of windowing broaden the main lobe, which effectively decreases the resolution, while decreasing the magnitude of the sidelobes.

As shown in Figure 4.2-5, using the Hamming window as an example, a 7.5 dB window causes the sidelobes to decrease in magnitude so that there is a 7.5 dB difference between the peak of the main lobe and the peak of the first sidelobe.

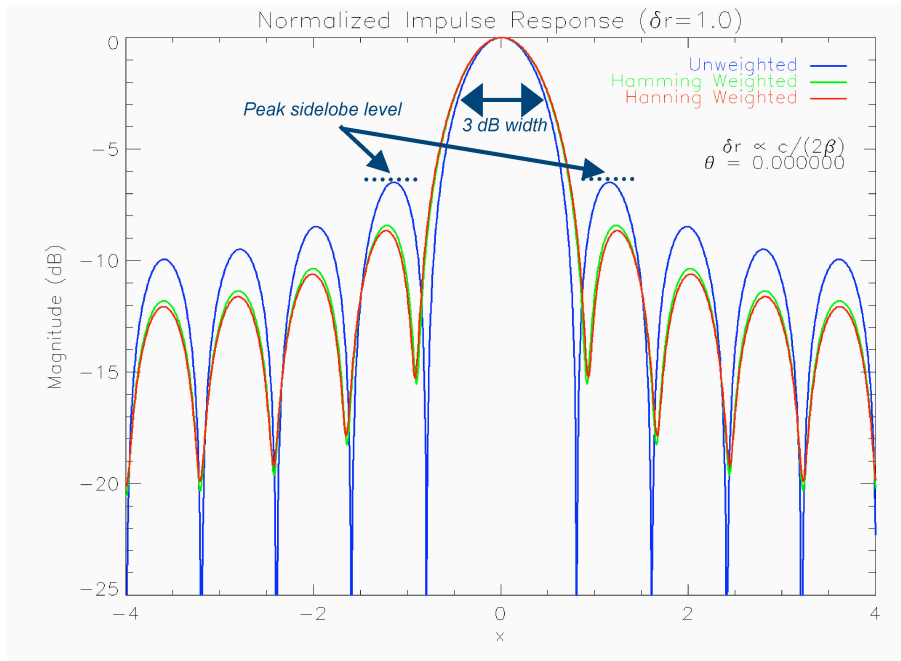


Figure 4.2-5 – Effects of different windowing techniques

Another issue with trying to match the IFSAR data with the simulated data is that in the actual IFSAR image, the corner reflectors do not stand out as brightly as they should for calibration targets. It could be that the post-processing steps were responsible for minimizing the returns of the corner reflectors or perhaps the reflectors never had had a high return due to the surrounding terrain or the fact that the 16-foot reflectors were mesh material, rather than solid material. Typically, corner reflectors are placed on a slab of concrete, a road, tarmac, or some other flat terrain that will produce the least amount of interfering clutter with their return since they are usually used as calibration targets for the sensor. The reflectors in the YOGI dataset were placed among trees and out in an open field, but always on grass terrain. It is possible that the side lobes from the terrain are such that they are interfering with the return of the corner reflectors, essentially dulling the return and making it difficult to discern which pixels constitute corner reflector. Furthermore, according to the test summary (Orloff et al, March 2004), on the day the IFSAR sensor was flown, the 16-foot corner reflectors were rotated so that they were facing south, and the look angle of the sensor was reported to be from the east. Therefore, since the radar was not looking directly into the corner reflector, the return may not have been as bright

as if it had been looking directly into it. In order to determine the difference in returns from a radar system pointing directly into the reflector as opposed to pointing at one of the sides of it, as it was the case in the YOGI collect, one last Xpatch simulation was run. The reflector was attributed with PEC material to keep the run time to a minimum and the look angle was set to be staring at one side of the reflector. The resulting SAR image is shown in Figure 4.2-7.

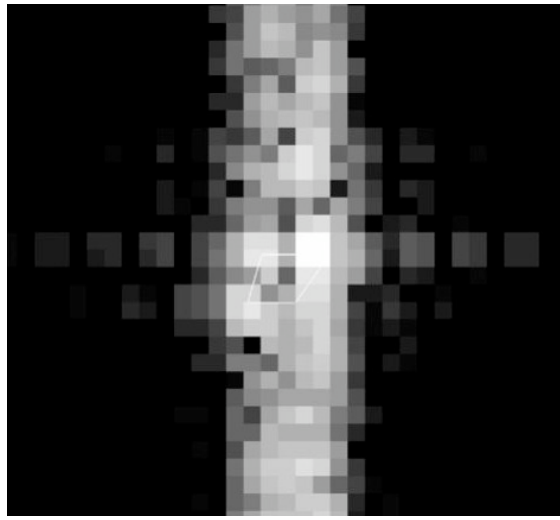


Figure 4.2-7 – Xpatch SAR image for radar pointed at side panel

It is inherently obvious that there are large differences in returns from a radar pointed at the inside corner of a reflector as opposed to the side panel. There is significant smearing in the azimuth direction, which is expected since the return will look the same along that direction since the reflector appears to be a flat panel to the radar system. A pixel comparison for a slice through this simulated image resulted in very low returns as opposed to the IFSAR data. In the case of this research, the returns from the radar pointed directly at the inside corner of the reflector exhibited better agreement with the real data than the image for the system pointed at a side panel. The main reason for this discrepancy is that the CAD model used in the Xpatch runs did not model the mesh material. When the radar is pointed at the inside corner, the energy is bouncing off the panels at an angle, so that while some of the energy is passing through the mesh, the rest is bouncing off the inside panels and returning to the receiving antenna. When the simulation was set to look at the side panel rather than the inside corner, the rays were pointing perpendicular to the panel, causing more of the energy to pass through the mesh, resulting in a

much lower return. Therefore, it would be necessary in future SAR simulations to model such material properties as the mesh in this corner reflector.

Figure 4.2-8 is meant as an example of how returns from corner reflectors typically manifest themselves as very bright returns against the background, which would have been the case in the IFSAR data had the sensor been flown to look into the inside corner of the reflector. The zoomed in portions of each of the reflectors demonstrate the presence of sidelobes, which are lacking in the IFSAR data. Information from these sidelobes can be useful in determining effects from phase error and windowing. The corner reflectors in Figure 4.2-8 also appear to be more similar to the signatures obtained from Xpatch for the case in which the sensor was pointed inside the reflector, indicating that perhaps the data set from the IFSAR sensor was a difficult set to try to model.

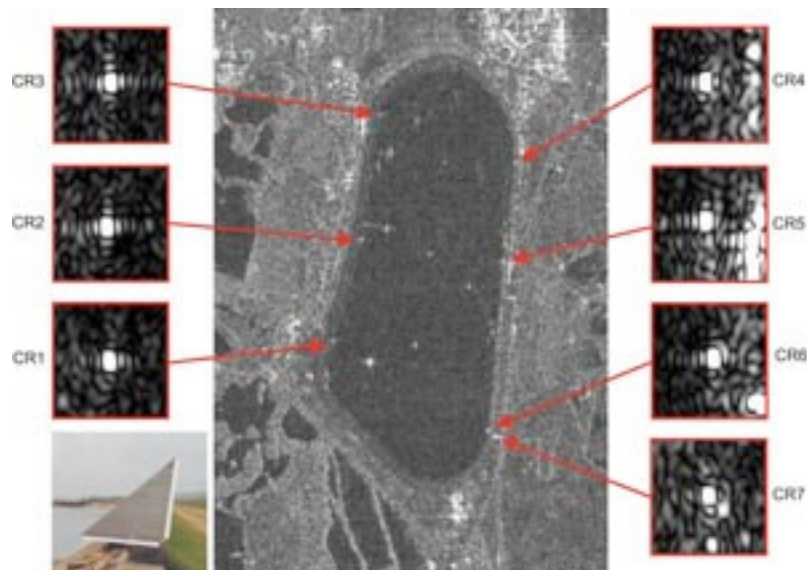


Figure 4.2-8 – Example of bright returns from corner reflectors (NPA Satellite Mapping, 2005)

5 Conclusions

This section will summarize the conclusions of this research based on the objectives and results. Included in this section are recommendations for future work based on the lessons learned in this research.

5.1 Electro-Optical Simulations

A CAD model of a simple scene involving two sizes of corner reflectors, two types of trees, and calibration panels to ease display issues was created in Rhino and converted to a format for use by DIRSIG. Using the information from the YOGI data collect regarding the electro-optical sensor, WARHORSE, DIRSIG was set up to model the sensor characteristics, flight characteristics, atmosphere, time of year and time of day, and latitudinal/longitudinal coordinates of the Fisher Creek scene. After multiple iterations varying such parameters as material attributes, texture, and atmospheric effects, the spectra from the different objects within the simulated data closely matched the WARHORSE spectra, with errors ranging from about 3-4%. The largest discrepancy between the data occurred at 760 nm, where a trough in the simulated data was much larger than in the real data, which is most likely the cause of most of the error.

This research demonstrates that it is possible to create the geometry for a scene that is based on real data, and model a real sensor that outputs images that are radiometrically accurate to the real data. The main issues encountered were a result of missing or unknown ground truth with regards to the specifics of the targets chosen to model in this research. For example, the material properties of the aluminum corner reflector were not reported and therefore a reasonable estimate had to be converged upon in order to get a close spectra match to the real data.

Another issue was a result of using DIRSIG 3.6 rather than DIRSIG 4.0, the newer version. This issue was that of material mapping. The corner reflector was actually a mesh material, which would have been possible to model using a material map where the holes were a null material. However, DIRSIG 3.6 does not have the capability to overlay material maps on a vertical surface, only a horizontal surface. Therefore, treating the aluminum as transmissive where the mesh existed in the real reflector was a less accurate way of modeling the material, and

hence resulted in some error between the real data spectra and the simulated spectra. Though the geometrical mesh in the real corner reflector resulted in holes in the shadows behind the reflector, these holes were too small to have been imaged by the WARHORSE sensor with 0.56m GSD. Therefore, attributing the reflector in DIRSIG with transmissive aluminum rather than building it in the CAD environment with the geometrical transparency would not have resulted in much error. However, in the case towards the center of the reflector where grass was most likely poking through the mesh during the data collection, the geometrical transparency rather than the optical transparency achieved through a transmissive material might have increased the accuracy of the comparisons.

5.2 Synthetic Aperture Radar Simulations

The SAR simulations proved to have more issues as this research approached the problem than the electro-optical simulations. Once the software was obtained and the initial installation bugs were sorted out, the run times encountered were anywhere from 30 hours to 100 days, making many of the planned simulations unusable, since it was not practical or feasible to wait 100+ days for the output. Therefore, the SAR simulations are lacking in diversity and content, since the most complicated simulation involved the corner reflector on a ground plane.

One of the objectives of this research was to determine if a common geometry could be run in both the electro-optical simulation tool and the SAR simulation tool. Though it was not possible to run the full geometry of the simple scene in the SAR simulation tool as was run in the EO simulation tool, it can be concluded that it is indeed possible to run the same geometry in each tool. Once a conversion tool was created to write the DIRSIG acceptable formatted CAD models into the Xpatch acceptable format, the simulation was set up like any other run, indicating that any CAD model can be run in Xpatch with a few minor conversions.

Though the simple scene with the corner reflectors, panels and trees was run with many different iterations for the EO simulations in DIRSIG, it was not successfully run in Xpatch. Throughout the course of this research effort, issues were encountered with the use of Xpatch. First, the delivery time for the software took much longer than originally expected, cutting its usable time for this research significantly. Once it was installed and working properly on the Sun machine allocated for its use, run times encountered were excessively long. For a corner reflector

on a simple ground plane, the run took approximately 35 hours. When any degree of complexity was added from there, the run progress was averaging 1% per day, which would have resulted in 100 days, a timeframe that was unreasonable for this research. Therefore, scenes more complicated than the corner reflector on a ground plane were not possible for this research.

The long run times associated with Xpatch are not common to all installations of Xpatch. The input page for the run that took 35 hours to complete, and its associated materials settings file, were sent to a user at AFRL (Air Force Research Laboratory), who was able to run it in approximately 3 minutes on a Linux based machine. The same input page was sent to an SAIC employee, who ran it as PEC material in 2 minutes and as aluminum material using the materials settings file in 4.5 hours, also on a Linux based machine. So even the longest run time experienced on a Linux machine of 4.5 hours is an improvement over 35 hours, and would be a reasonable amount of time for a simulation. This indicates that perhaps the Sun machine was not the best system on which to run Xpatch for this research. The user at AFRL indicated that all Xpatch runs are done on Linux based machines because they outperformed Sun machines.

As mentioned in the results section, it was determined through long run times and information gathered from AFRL resources who have used Xpatch that it is not a tool best suited for simulated scenes. One of the reasons for this is that it does not model electrically small objects as well as it does for electrically large objects. Since many of the objects in a scene are electrically small, such as grass, tree leaves and other small targets, Xpatch cannot as accurately predict what the SAR image should be for such objects.

Another possible SAR simulation tool that might be researched for future SAR simulations is a tool described in the research of (Mametsa et al, 2002). It is a three-dimensional SAR simulation package under development between the Electromagnetism and Radar Department of ONERA and the OKTAL SE Company. It seems to be better suited for scene simulations, rather than just object simulations.

Another of the objectives laid out in the introduction was to not only correctly render a scene in both tools but to compare it to real data. These comparisons were shown in the results section, and though there were not very many SAR simulations to compare, it was shown that fairly accurate data could be simulated in Xpatch for a simple corner reflector as compared to the reflector in the IFSAR data.

5.3 Data Fusion

Part of the desire of this research was to progress far enough into the simulations in both EO and SAR to attempt some type of data fusion. Due to limitations with Xpatch as it was set up and run for this research as well as time constraints, it was not possible to explore fusion in this research. However, there are many resources in the community that address different types of data fusion, including (Staelin et al), (Hsu et al, 1999), and (Chang et al, 2004). Depending on the scene, sensor types, and desired exploitation of the imagery, there are a variety of ways to approach the data fusion problem in order to obtain a synergistic combination of data among the images.

5.4 Recommendations for Future Work

Throughout this document it has been noted that one of the objectives of this research was to determine whether or not it was possible to get a common geometry working in an EO simulation tool as well as a SAR simulation tool. It has been demonstrated that this is indeed possible and rather straightforward to get the CAD format into a working format for the DIRSIG and Xpatch tools. However, in doing so, it was also determined that using Xpatch generates its own set of issues. Many months were spent waiting on the delivery of the Sun machine-licensed version of Xpatch. Once it was obtained, slow run times and further research revealed that it typically runs much faster on Linux machines. Two more months were spent awaiting delivery of the Linux based Xpatch software, which did not arrive in time for use in this research. However, in waiting for the Linux-based software, it was determined through communications with AFRL personnel modeling SAR simulations that though Xpatch models objects very accurately, it is not the best-suited tool for scenes. Therefore, it is recommended that future research utilize a SAR simulation tool more tailored for scenes. In addition to using another tool, it is suggested that the tool already be purchased and in place before any research is planned for its use so that time is not wasted awaiting its delivery.

Once a more appropriate SAR simulation tool is encountered and found to utilize a format that can be converted from a Rhino or similar CAD format, a more complex scene from

the one used in this research should be tested. Though the corner reflector was found to be compatible in both tools, nothing more complex was ever successfully tested due to unreasonably long run times. Therefore it is only an assumption at this point that an entire scene with complex objects and backgrounds could be successfully modeled in both tools accurately.

Upon determining the robustness of the simulation tools for modeling a complex scene, research should be done on what types of data fusion are most appropriate for combining the EO and SAR data. The objective in fusing the data would be to obtain more information from a single fused image than from either of the separate images. Therefore, it must be determined what information is most useful to an image analyst from the EO and SAR images and using that information, fuse them in a way that augments the useful information.

Lastly, if it is possible to become involved on a multi-sensor data collection effort, it is recommended that extensive ground truth be obtained on any objects that will later be modeled in the simulation tools. This would include any material properties inherent to each of the tools; in the case of the EO and SAR tools, reflectance properties and dielectric properties would be most useful.

6 References

Andersh, D.J., Hazlett, M., Lee, S.W., Reeves, D.D., Sullivan, D.P., and Chu, Y., "XPATCH: A High Frequency Electromagnetic-Scattering Prediction Code and Environment for Complex 3D Objects," IEEE Antennas and Propagation, vol. 36, pp. 65-69, 1994.

Astrocappella website <http://www.astrocappella.com/>

Blevins, Daniel, "Linear SAR Signal Models," SAR Course Reference Slides, 2004.

Brown, Scott, Personal Communications, 2005.

Campbell, James B. "Introduction to Remote Sensing." The Guilford Press, New York, 1996.

Carrara, Walter G., Goodman, Ron S., Majewski, Ronald M., "Spotlight Synthetic Aperture Radar Signal Processing Algorithms," Artech House, Inc., Massachusetts, 1995.

Castelloe, Michael W., Munson, Jr., David C. "3-D SAR Imaging via High-Resolution Spectral Estimation Methods: Experiments with XPATCH," IEEE, 1997.

Chang, Yang-Lang, Han, Chin-Chuan, Ren, Hsuan, Chen, Chia-Tang, Chen, K.S., Fan, Kuo-Chin. "Data fusion of hyperspectral and SAR images," Optical Engineering, Vol. 43 No. 8, August 2004.

Davis, J.R., "Aluminum and Aluminum Alloys," ASM International, 1993.

DIRSIG User's Manual Release 3.6, Digital Imaging and Remote Sensing Laboratory, RIT, 2004.

DPI Website, <http://www.dpi.inpe.br/spring/teoria/radar/radareng.htm>, 2004.

Georgia Tech Research Institute website,
http://www.gtri.gatech.edu/eoeml/sats/area_phenom.html, 2004.

Hazlett, Michael A., Andersh, Dennis J., Lee, S.W., Ling, H., Yu, C.L. "XPATCH: A High Frequency Electromagnetic Scattering Prediction Code Using Shooting and Bouncing Rays," SPIE Vol. 2469.

Hsu, Su May, Kerekes, John P., Burke, Hsiao-hua, Crooks, Steve. "SAR and HSI Data Fusion for Counter CC&D." IEEE, 1999.

Integrated Publishing Website,
http://www.tpub.com/content/aerographer/14271/css/14271_61.htm, 2004.

JPL AIRSAR website <http://www.tsgc.utexas.edu/trcp/airsar.html>, 2004.

Kerekes, John., Crabtree, Robert. "Mathematical Modeling and Fusion of Hyperspectral and Synthetic Aperture Radar Data in Open and Urban Landscapes," A white paper in response to Air Force Research Lab Broad Agency Announcement 04-03-SNK, Amendment 003, 24 May 2004.

Lillesand, Thomas M., Kiefer, Ralph W. "Remote Sensing and Image Interpretation." John Wiley & Sons, Inc., New York, 1994.

Mahafza, Bassem. "Introduction to Radar Analysis." CRC Press, Florida, 1998.

Mametsa, H.J., Rouas, F., Berges, A., Latger, J., "Imaging Radar Simulation in Realistic Environment Using Shooting and Bouncing Rays Technique." SAR Image Analysis, Modeling, and Techniques IV, Proceedings of SPIE Vol. 4543, 2002.

MicroImages, Inc. "Interpreting Digital Radar Images with TNTmips ®." Nebraska, 2001.

MSTAR Data Collection #2, Sandia National Laboratory, 1998.

NASA JPL website <http://southport.jpl.nasa.gov/desc/imagingradarv3.html>, 1996.

National Severe Storms Laboratory, Polarimetric Radar Research website
<http://cimms.ou.edu/~schuur/radar.html>, 2003.

Nicodemus, Fred E., "Self-study manual on optical radiation measurements: Part 1 – Concepts, Caps. 1 to 3," NBS Technical Note 910-1, U.S. Dept. of Commerce, National Bureau of Standards, U.S. Printing Office, Washington, DC.

NPA Satellite Mapping, <http://www.npagroup.com>, 2005.

Orloff, S., Kerekes, J., "YOGI Experiment Coordinated Test Summary," MIT Lincoln Laboratory HTAP Report 15, Lexington, MA, 8 March 2004.

Orloff, S., Kerekes, J., "Yellowstone Optical and SAR Ground Imaging (YOGI) Terrain Characterization Problem Set," MIT Lincoln Laboratory, HTAP-23 Project Report, 6 December 2004.

Peterson, Erin D. "Validation and Verification of Surface and Buried Landmine Signatures in DIRSIG." M.S. Thesis, Rochester Institute of Technology, 2004.

PROFC Website, <http://www.profcl.udec.cl/~gabriel/tutoriales/rsnote/cp4/cp4-3.htm>, 2005.

Richards, John A. "Synthetic Aperture Radar." Encyclopedia of Optical Engineering, 2003.

SAIC Website, "SAIC Releases New Version of XPATCH™" March 19, 2001,
<http://www.saic.com>.

Schott, John R. "Remote Sensing: The Image Chain Approach." Oxford University Press, New York, 1997.

Skolnik, Merrill. "Radar Handbook," McGraw-Hill Publishing Company, New York, 1990.

Space Computer Corporation, Autonomous Real-Time Target Detection System for UAV Applications website, <http://www.spacecomputer.com/WHorse.html>, 2004.

Staelin, David H., Kerekes, John P. "Combined Microwave and Optical Atmospheric Remote Sensing Techniques: A Review." Combined Optical-Microwave Earth and Atmosphere Sensing, Conference Proceedings, Second Topical Symposium on 3-6 April 1995.

Stellman, Christopher M., Ochowski, Frederick M., Michalowicz, Joseph V. "WAR HORSE (Wide Area Reconnaissance – Hyperspectral Overhead Real-time Surveillance Experiment)." Automatic Target Recognition XI, SPIE Vol. 4370, 2001.

Stimson, George W. "Introduction to Airborne Radar." SciTech Publishing, Inc., New Jersey, 1998.

Sutherland, R.H., Cowan, M.I. "COMPASS Sensor Modelling Application." 1st EMRS DTC Technical Conference, Edinburgh 2004.

Tapley, Ian J. "Radar Imaging." Geophysical and Remote Sensing Methods for Regolith Exploration, CRCLEME Open File Report, 2002.

Traffic Radar Handbook, <http://copradar.com/preview/xappA/xappA.html>, 2005.

Vexcel website <http://www.vexcel.com/products/scatter.html>, 2004.

Walker, B., Sander, G., Thompson, M., Burns, B., Fellerhoff, R., Dubbert, D. "A High-Resolution, Four-Band SAR Testbed with Real-Time Image Formation." Sandia National Laboratories.

Xpatch Training Course, SAIC, Champaign, IL, 2004.

Xpatch 4.7.16-3 User's Manual, 2004.

Yang, Y.E., Ewe, H.T., Hsu, C.C., Wang, L., Shih, S.E., Ding, K.H., Kong, J.A., Shin, R.T., Nguyen, H., Ho, J.YI, O'Neill, K. "A GIS-Driven Interactive Radar Image Simulation Using EMSARS Model." IEEE, 1994.